

# A new Phenomenon: Glass Paramagnetism. Further Experimental and Theoretical Details

Giancarlo Jug<sup>a,b,c</sup> and Sandro Recchia<sup>a</sup>

<sup>a</sup>Dipartimento di Scienza ed Alta Tecnologia  
Università dell'Insubria, Via Valleggio 11, 22100 Como (Italy)

<sup>b</sup>INFN – Sezione di Pavia, Italy

<sup>c</sup> To.Sca.Lab, Dipartimento di Scienza ed Alta Tecnologia, Università dell'Insubria

November 25, 2021

## Abstract

**In a recent manuscript, the discovery of a new phenomenon in glasses has been reported: *glass paramagnetism*, that is the intrinsic magnetisation developed by a substance that has failed to crystallise in a temperature quench when placed in an external magnetic field. The field- ( $H$ ) and especially the temperature- ( $T$ ) dependence of the intrinsic magnetisation  $M_{intr} = M_{intr}(H, T)$  is very unexpected, with broad peaks developing for high  $H/T$  and marked  $T$ - oscillations at fixed  $H$  for intermediate-to-high temperatures. In this work we present details on the samples, new data for other glassy systems and especially the theoretical background that is capable of explaining most of the experimental data. New phenomena are however emerging from these data, for example a deviation from the Curie-like behaviour of the magnetic susceptibility ( $M_{intr}/H$  at low fields) due to the glassy structure alone as well as evidence for new and intriguing quantum coherence effects at the lowest temperatures.**

## Contents

- A. The Samples
- B. Polycluster and Extended Tunneling Models for Glasses
- C. Some More Data Fitting Results
- D. Further Discussion about Curie Law and Comparison with ETM-Theory
- E. The  $M_{intr}$  Temperature Oscillations and the High Field Limit
- F. Novel Quantum-Coherence Phenomena
- G. Final Conclusions, Authors and Acknowledgements

**Introduction.** This manuscript is the continuation of a shorter, parent article and readers are referred to the Introduction of that article for background information. Hereafter, the Parent Article [1] is throughout indicated as the PA; MS stands for Mass Spectroscopy. PI is the Principal Investigator (GJ).

**A. The Samples.** Fig. 1(a) shows three of our four glass samples, measured in the Quantum Design SQUID magnetometer. Together with chips from the BK7 prism (what remains of it) on the left, we produced shards from a shattered Schott’s Duran beaker identical to the one pictured in Fig. 1(c). We insist on this issue, the green coloration, because it invalidates claims made from naive LL SQUID-measurements that Fe is contained only as  $\text{Fe}^{3+}$  (coloring yellow) in ordinary multi-silicate glasses. It is not, it is predominantly  $\text{Fe}^{2+}$  (coloring green) and this enhances the discrepancy between the LL-SQUID-ascertained  $n(\text{Fe})$  and the true  $n_{MS}(\text{Fe})$  value. This strenghtens the case for the existence of an intrinsic, glassy state magnetisation.

**B. Polycluster and Extended Tunneling Models for Glasses.** Alternatives to the popular Zachariasen-Warren CRN model of glasses [2, 3] have been occasionally proposed in the literature. The cybotactic-groupings model of Valenkov-Porai-Koshits-Lebedev [4, 5] (for recent reviews, see [6, 7, 8]), the modified-CRN model of Greaves [9] and the polycluster model of Bakai [10, 11] are the closest in spirit to the one independently proposed by the PI [12], except that the cybotactic and Greaves versions both consider better-ordered and less-ordered regions as highly inter-penetrating each other. In the polycluster model, like in the PI’s own [12], the better-ordered regions are solid-like compact objects that get to be jammed together below  $T_g$  and contain “voids” filled with mobile, fluid-like particles (ions or molecules) from the surviving supercooled melt. In a nutshell, the clusters or RER are failed nanocrystals almost monodispersed in size and randomly closed-packed at low enough  $T$ , their network percolating the entire system (see Fig. 5(a) in the PA and Fig. 2 below). Vogel in Refs. [13, 14] and especially in Ref. [15] (see also Section D) as well as Zarzycky [16] have provided dramatically convincing HRTEM images of the hidden granularity of glasses. See however [17] for a distinction between truly dynamical (ca. 1 nm size) heterogeneities – characterising single-component systems – and quasi-static heterogeneities (10s to 100s of nm in size) typical of the multi-component systems. We focus on the fluid-like particles from the remaining supercooled melt in the “voids”, which are of a highly complex nature, especially in the multi-component glasses where micro-phase separation between network-forming (NF, e.g.  $\text{SiO}_2$ ,  $\text{Al}_2\text{O}_3$ ,  $\text{B}_2\text{O}_3$ , ...) and network-modifying (NM, e.g.  $\text{Na}_2\text{O}$ ,  $\text{K}_2\text{O}$ ,  $\text{BaO}$ , ...) components has long been known to take place [13, 14, 16]. A couple more HRTEM pictures are in Fig. 2. The idea, then, is that the NM (good crystal-formers’) atomic species tend to segregate in the RER while the NF (good glass-formers’) species tend to segregate – locally and only in part – in the voids. In any event (even if the opposite happens), it is natural to believe that a highly-heterogeneous schematic situation like that in Fig. 6(b) in the PA – when needed – better characterises glass structure at medium-range (or mesoscopic) scales than the CNR model. We stress that the polycluster model is clearly only an effective model, glossing over considerable (and unexplored) detail.

Next, the shape and size of each void, or pore, between four RER (tetrahedral void) can be estimated from HRTEM images like in Fig. 6(a) (PA) and in Fig. 2 – or, better, from fitting low-temperature heat-capacity and magnetisation data to this theory – to be of distorted tetrahedral minimal shape and having volume (if  $2\xi$  is the size of a typical RER):

$$V_{t\text{-void}} = \left\{ \frac{2\sqrt{2}}{3} - \frac{4}{3} \arccos\left(\frac{23}{27}\right) \right\} \xi^3 \simeq 0.208 \xi^3. \quad (1)$$

This for  $\xi \simeq 30$  nm, a typical value for BK7 as it turns out [12], gives a volume of some  $5.6 \times 10^6 \text{ \AA}^3$  and hence a linear size of some  $3.62 \times 10^2 \text{ \AA}$  for the tetrahedron’s side. This is enough to accommodate some 400 atomic species on each tetrahedron void’s face in a packed monolayer fashion. These species can be reasonably considered to be  $\text{O}^-$  species adsorbed on each face from the melt in the void, and these negative particles will be highly correlated and electrostatically interacting, so that not all available tetrahedron-void face’s adsorption sites will be occupied. Let us say that only some  $N_{tunn}$  will be present as dangling  $\text{O}^-$  bonds on each face. Values of  $N_{tunn}$  in the range 20 to 600 have in fact been extracted from applications of the Extended Tunneling Model (ETM) below to a plethora of low-temperature experimental data [12, 18, 19]. The void’s shape is clearly only topologically tetrahedral, distortion is everywhere.

Fig. 3(a) shows (idealized, in practice all will be random) the packing of the compact RER (strickly speaking, just below  $T_g$  idealisation) and the creation of a tetrahedral “void” which in practice will be filled with many charged and mobile particles. There are octahedric and cubic distorted voids too, but in order to keep the



(a)



(b)



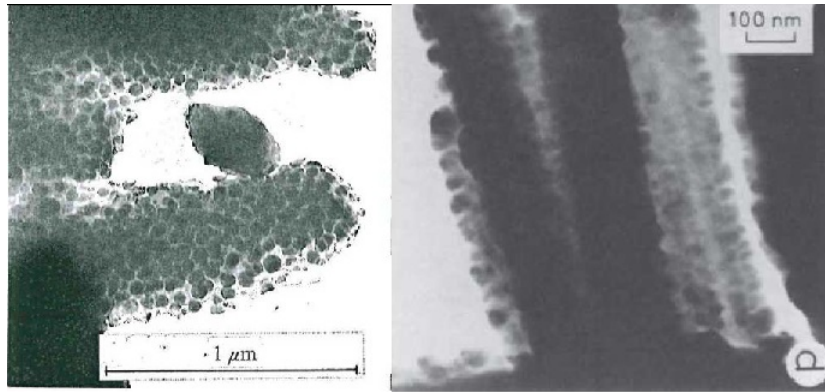
(c)

Figure 1: (a) Some of our glass samples (from the left: BK7 (remaining prism), Duran 79.5 mg, BAS-p 27.9 mg, as explained in the PA text). The base-lens (made of ordinary window glass, diameter 57 mm) is displayed to show the green coloration due to  $\text{Fe}^{2+}$ -predominance. (b) Shards from the very same Duran glass beaker from which we obtained the sample in the middle of (a); the greenish tinge of this glass is clearly visible along the edges. (c) Schott's Duran beaker, an identical copy of which we shattered to make our Duran samples; noticeable is the green coloration along the longest optical path (also visible in the Duran shard at the centre of (a), front upper rhs-corner and front bottom edge, and along the edges of the shards in (b)). Illumination was with white LED light.

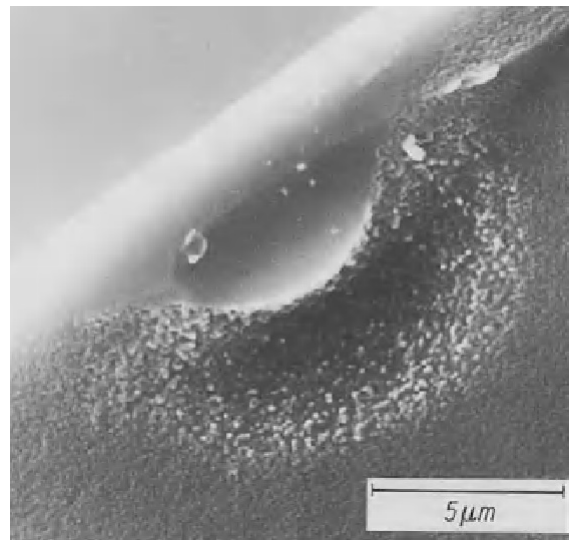
theory simple these other void topologies will be ignored for now. The charged particles inside each void should be described by the microscopic Hamiltonian:

$$\mathcal{H}_{micr} = \sum_{i=1}^N \frac{p_i^2}{2m_i} + \sum_{i>j} \frac{q_i q_j}{r_{ij}} + \sum_{b=1}^4 \frac{q_i q_{J_b}}{R_{i,J_b}} + \sum_{b,b'} \frac{q_{J_b} q_{J_{b'}}}{R_{J_b J_{b'}}} + \dots \quad (2)$$

where  $i, j$  are atomic particles inside the void,  $m_i$  are their masses,  $J_b$  labels a solid-like particle inside one of the four “solid clusters” (the RER) surrounding the void,  $q_i, q_{J_b}$  are the charges of the particles in the void and inside the blobs, respectively, and  $r_{ij}, R_{i,J_b}, R_{J_b J_{b'}}$  are the distances between all these pairs of



(a)



(b)

Figure 2: (a) Two more HRTEM images showing the polycluster structure of network glasses. Left panel: the  $(\text{B}_2\text{O}_3)_{0.75}(\text{PbO})_{0.25}$  (wt%) glass system, its granularity being exacerbated by micro-phase separation. Right panel:  $\text{a-SiO}_2$ . In both cases sample preparation in the form of thin slices for EM-imaging enhances, through partial stress-release, the size of clusters with respect to bulk systems. From [16]. (b) The HRETM image of the fractured surface of the same  $\text{Li}_2\text{O-SiO}_2$  glass as in Fig. 6(a) of the PA: the granularity of the glass' bulk as well as the cellular structure on the fracture's surface are quite evident. From [14].

interacting atomic particles. The last term is in practice redundant, as the positions of solid-like particles changes little, the third term ought to include all of the RER in the system, but the truth of the matter is that such microscopic model is clearly intractable (even through computer simulation). Therefore, one resorts to an effective Hamiltonian, initially focusing on a group of the particles in the void: those deposited on the surface of one RER (e.g. RER n.1 in Fig. 3(b)) which are presumably mostly  $\text{O}^-$  dangling bonds.

One then replaces these highly correlated particles with a single *effective* “particle” of mass  $M$ , charge  $Q$  subjected to an effective potential  $V_{eff}$  that, as shown in Fig. 4, will be characterized by three minima in correspondence with the three (n. 2-3-4) RER facing the chosen (n.1) effective-particle zone. The impossible Hamiltonian in Eq. (2) then becomes tractable [20]:

$$\mathcal{H}_{eff} \approx \frac{P_b^2}{2M} + V_{eff}(\mathbf{R}_b) \quad (3)$$

where  $\mathbf{R}_b = (x, y, z)_b$  is a coordinate for the effective-particle  $b$  on the plane of the opposite triangular RER-arrangement and  $z_b$  its (fixed, in practice) distance from that plane. This holds for each “particle”  $b$  ( $=1,2,3$  or  $4$ ) defined on each of the RER-faces involved in that void. However, it is likely that the character of the effective particle will change from surface-like (2D in nature) to void-like (3D) as temperature drops considerably (see Section F). Indeed, through adsorption of mobile void-species on the RER surfaces, the RER get to grow and compactify at the expense of the fluid-like species in the void. Thus, one can expect that at the lowest temperatures the effective particle will characterise the whole of the void’s atomic particles’ distribution and the  $V_{eff}(\mathbf{R})$  effective potential will acquire a four-welled tetrahedral configuration.

At this point one is set to represent the (unknown, except for its topology) effective potential  $V_{eff}(\mathbf{R})$  in terms of the quantum-mechanical basis  $|\alpha\rangle$ ,  $\alpha=1, 2, 3$ , of its three wells, to get  $\mathcal{H}_{eff}$  in matrix form and with a minimal number of parameters:

$$\mathcal{H}_{3LS} = \langle \alpha | \mathcal{H}_{eff} | \beta \rangle = \begin{pmatrix} E_1 & D_0 & D_0 \\ D_0 & E_2 & D_0 \\ D_0 & D_0 & E_3 \end{pmatrix} \quad (4)$$

the  $E_1, E_2, E_3$  being the energy asymmetries between the wells (chosen so that  $E_1 + E_2 + E_3 = 0$  for each tunneling system (TS)) and  $D_0$  is the most relevant tunneling amplitude (through saddles, in fact). This three-level system (3LS) Hamiltonian is the natural generalisation of the popular Standard Tunneling Model’s (STM) 2LS Hamiltonian [21],

$$\mathcal{H}_{2LS} = \begin{pmatrix} \Delta/2 & \Delta_0/2 \\ \Delta_0/2 & -\Delta/2 \end{pmatrix} \quad (5)$$

( $\Delta$  being the energy asymmetry and  $\Delta_0/2$  the tunneling amplitude) and has the advantage of readily allowing for the inclusion of a magnetic field  $B = \mu_0 H > 0$ , when coupling orbitally to the tunneling “particle” having effective charge  $Q$ :

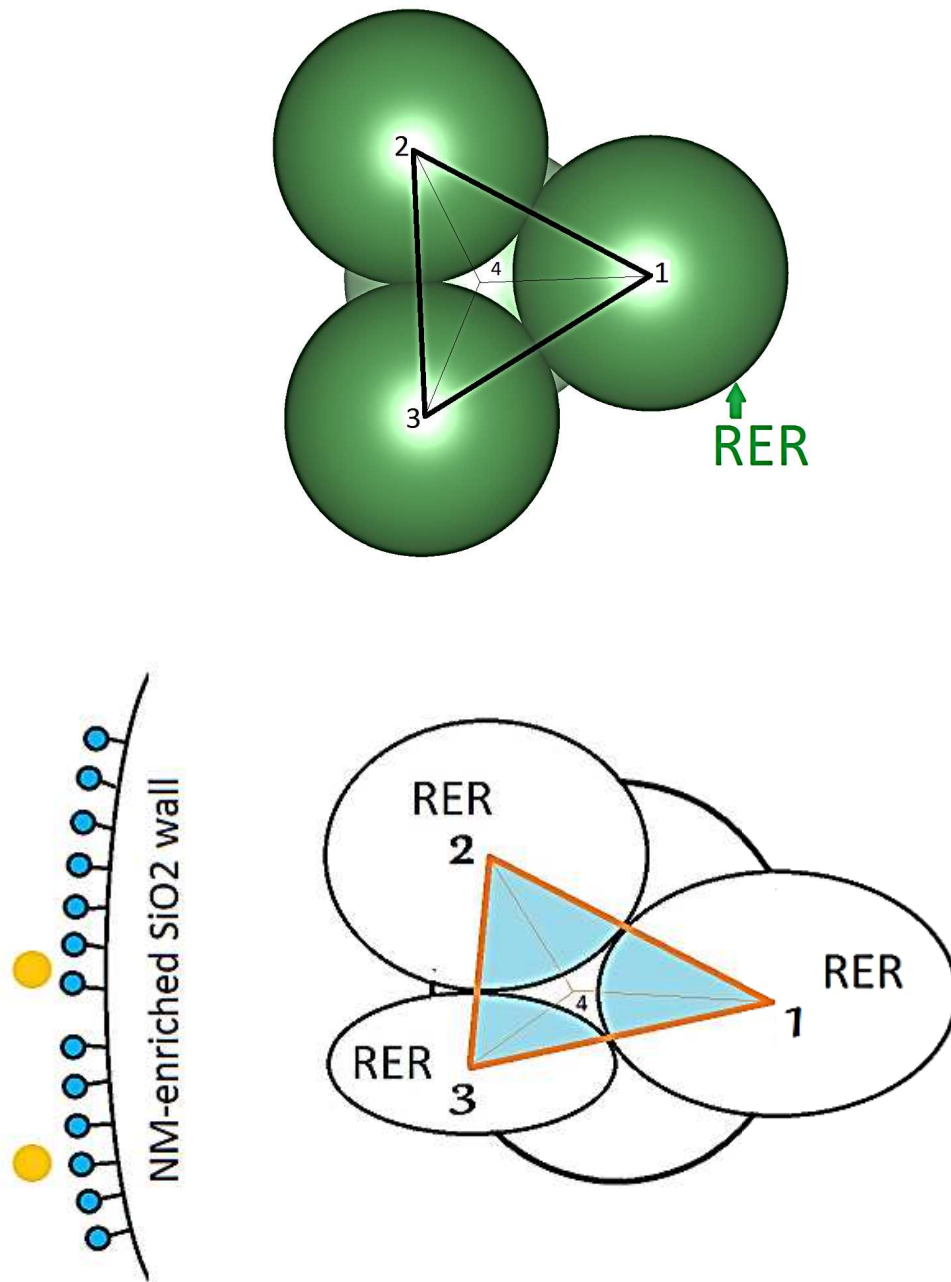
$$\mathcal{H}_{3LS}(B) = \begin{pmatrix} E_1 & D_0 e^{i\varphi/3} & D_0 e^{-i\varphi/3} \\ D_0 e^{-i\varphi/3} & E_2 & D_0 e^{i\varphi/3} \\ D_0 e^{i\varphi/3} & D_0 e^{-i\varphi/3} & E_3 \end{pmatrix}. \quad (6)$$

Here  $\varphi/3$  is the Peierls phase for the tunneling particle through a saddle in the presence of a magnetic field, and  $\varphi$  is the Aharonov-Bohm (A-B) phase for a tunneling loop, given by the usual formula ( $\phi_0$  is the electron’s flux quantum):

$$\varphi = 2\pi \frac{\Phi}{\Phi_0}, \quad \Phi_0 = \frac{h}{Q} = \phi_0 \frac{e}{Q}, \quad \text{where } \phi_0 = \frac{h}{e} \quad (7)$$

$\Phi_0$  being the appropriate flux quantum ( $h$  is Planck’s constant) and  $\Phi = \mathbf{B} \cdot \mathbf{S}_\Delta$  the magnetic flux threading the area  $S_\Delta$  offered by the tunneling paths of the “particle” in this simple quantum-mechanical model. The energy asymmetries  $E_1, E_2, E_3$  typically enter through their combination  $D \equiv \sqrt{E_1^2 + E_2^2 + E_3^2}$ . One can easily convince oneself that if such a multi-welled potential is used with the standard parameter distribution for the STM,  $\mathcal{P}_{3LS}(\{E_i\}, D_0) = \bar{P}/D_0$  (the analogous of  $\mathcal{P}_{2LS}(\Delta, \Delta_0) = \bar{P}/\Delta_0$  popular for the 2LS), for the description of the generic TS parameters’ distribution, one would then obtain essentially the same physics as for the STM 2LS-description. In other words, there would be no need to complicate the minimal 2LS description in order to study glasses at low temperatures, unless structural heterogeneities of the RER type and a magnetic field are present. Without the RERs, the interference from separate tunneling “particle” paths is likely to give rise but to a very weak A-B effect. Hence, it will be those TS nesting in the RERs’ voids that will give an enhanced A-B effect and these TS can be minimally described though Hamiltonian (6) and with the new parameters’ distribution:

$$\mathcal{P}_{3LS}^*(E_1, E_2, E_3; D_0) = \frac{P^*}{D_0(E_1^2 + E_2^2 + E_3^2)} \quad (8)$$



(b)

Figure 3: (a) tetrahedral void (octahedric and cubic voids are also present, but ignored for now) between RER, idealised as perfect spheres (which they are not). The actual space available to the mobile particles is that of the tetrahedron having vertices 1-2-3-4 minus the space occupied by the RER inside the tetrahedron. This space has volume  $V_{t-void} \simeq 0.208 \xi^3$  where  $\xi$  is the typical ideal-RER “radius” ( $2\xi$  is its linear size). (b) Schematic representation of RER void’s coating by  $O^-$  species (dangling bonds on light blue surfaces of more realistic, ellipsoidal RER shapes, delimiting the void) as exemplified in the particular drawing on the left: blue species  $O^-$ , golden species  $Si^{4+}$  or other NM-cation approaching and eventually adsorbing on the RER wall, causing it to grow and to attract replacement  $O^-$  from the surviving melt in the void. There is naturally a coating (not shown) on RER n.4 too.

enforcing the quasi-ordered character of the RER internal structure [22, 23]. It is at this point, in fact, that the scenario for glasses envisioned by Lebedev [5], Porai-Koshits [4], Greaves [9], Gaskell [7], Wright [8] and Bakai [10, 11] (as well as the PI's own [12, 24], of course) gets to be implemented. The new, magnetic-sensitive TS are named ATS (Anomalous Tunneling Systems) and are not 2LS (the ATS have a robust collective nature, while the 2LS are almost exclusively atomic). We remark that the incipient “crystallinity” of the RER [22, 23] calls for near-degeneracy in  $E_1, E_2, E_3$  simultaneously and not for a single one of them, hence the correlated form of (8). Other descriptions, with full tetrahedral four-welled potentials for the TS nested in the RER are possible and lead to the same physics [25] as from Eqs. (6) and (8) above. It is important to remark that a distribution  $\mathcal{P}_{3LS}^*(E_1, E_2, E_3; D_0)$  imposing sharp zero values for the asymmetries  $\{E_i\}$  (that is, enforcing  $E_1^2 + E_2^2 + E_3^2 = 0$ ) would lead to no magnetic effects at all. Hence these effects are not consequences of true crystallinity, but only of a local ordering-enhancement (such as in the cybotactic-grouping vision of melt-quenched glasses or in the RER-scenario).

The next important consideration is that the ATS appear to be rather diluted entities in the glass, hence the tunneling “particles” are embedded in a rather complex charged-particle medium. This embedding however means that the rest of the material takes a role in the tunneling of the ATS effective “particle”, which is not moving in a simple vacuum. Sussmann [26] has shown that this leads to local trapping potentials that (for the case of triangular and tetrahedral *perfect* symmetry) must be characterised by a degenerate ground state. This means that as a consequence of the embedding and of the many omitted contributions in Eq. (2) to be replaced by Eq. (3), our minimal model (6) must be chosen with a positive tunneling parameter:

$$D_0 > 0, \quad (9)$$

where of course degeneracy is always removed by weak disorder in the asymmetries. Such choice for the tunneling parameter goes completely unnoticed in the 2LS STM. With this description, the spectrum of the energy levels of a single ATS (supposed to be associated with the  $N_{tunn}$  atomic units active on each distorted tetrahedron's face) has the form reproduced in Fig. 7(c) (left panel, PA). The intrinsic near-degeneracy of (8) implies that this model can be used in its  $D/D_0 \ll 1$  limit, so long as the magnetic field is “weak” (i.e.  $\varphi \ll 1$ ) which in turn produces for low enough temperatures an *effective* magnetic-field dependent 2LS and greatly simplifies the analysis together with the limit  $\varphi \rightarrow 0$  which can be used for relatively “weak” magnetic fields. The above Extended Tunneling Model (ETM) consists then in a collection of independent, non-interacting 2LS described by the STM and 2LS-like non-interacting 3LS of internal collective nature described by Eqs. (6) and (8) above and in the said  $D/D_0 \ll 1$  and  $\varphi \rightarrow 0$  limits. The 3LSs are quasi-particles nested in the voids between the RER and the magnetic-field insensitive 2LS are distributed in the RER and (as it turns out) overwhelmingly around their contact interfaces (see Section F). In the said limits, a reasonable approximate form for the lower energy gap is of the simple form [24]  $E = \sqrt{D^2 + D_0^2 \varphi^2}$ ; for higher fields this can be easily corrected (see below) still to make a manageable analytic theory.

At this point, the contribution to the magnetisation from the tunneling currents located (initially, at least) on the faces of the distorted tetrahedra (one tetrahedron per each RER “void”) can be calculated from the ETM above described, using standard quantum statistical mechanics. As already shown in [27], in the limit of weak fields the following expression can be used (for a given  $\mathbf{B}$ -direction):

$$M_{intr}^{tunn}(T, B) = \pi P^* n_{ATS} \frac{1}{B} \left\{ \int_{E_{c1}}^{E_{c2}} dE \tanh\left(\frac{E}{2k_B T}\right) \ln\left(\frac{E^2 - D_{0min}^2 \varphi^2}{D_{min}^2}\right) + \int_{E_{c2}}^{\infty} dE \tanh\left(\frac{E}{2k_B T}\right) \ln\left(\frac{E^2 - D_{0min}^2 \varphi^2}{E^2 - D_{0max}^2 \varphi^2}\right) \right\} \quad (10)$$

where:  $D_{min}, D_{0min}$  and  $D_{0max}$  are material-dependent cutoffs of the ATS parameter distribution, Eq. (8);  $E_{c1} = \sqrt{D_{min}^2 + D_{0min}^2 \varphi^2}$  and  $E_{c2} = \sqrt{D_{min}^2 + D_{0max}^2 \varphi^2}$  are special points in the density of states of the ATS spectrum; finally  $n_{ATS}$  is the ATS concentration (quantity always convoluted with  $P^*$ , the single ATS energy-distribution parameter which when normalized gives the somewhat undetermined relationship  $1/P^* = 2\pi \ln\left(\frac{D_{0max}}{D_{0min}}\right) \ln\left(\frac{E_{max}}{D_{min}}\right)$ ,  $E_{max}$  being linked to the (unknown) single ATS-well attempt frequency: in practice,  $P^*$  is of order  $1/2\pi$ ). Eq. (10) needs to be averaged over ATS orientations with respect to  $\mathbf{B}$ . When the magnetic field is not so weak (this is determined by a material-dependent characteristic field  $B^*$  [28, 27]) the above expression can be cured by simply shifting:

$$\varphi^2 \rightarrow \varphi^2 \left(1 - \frac{1}{27} \varphi^2\right) \quad (11)$$

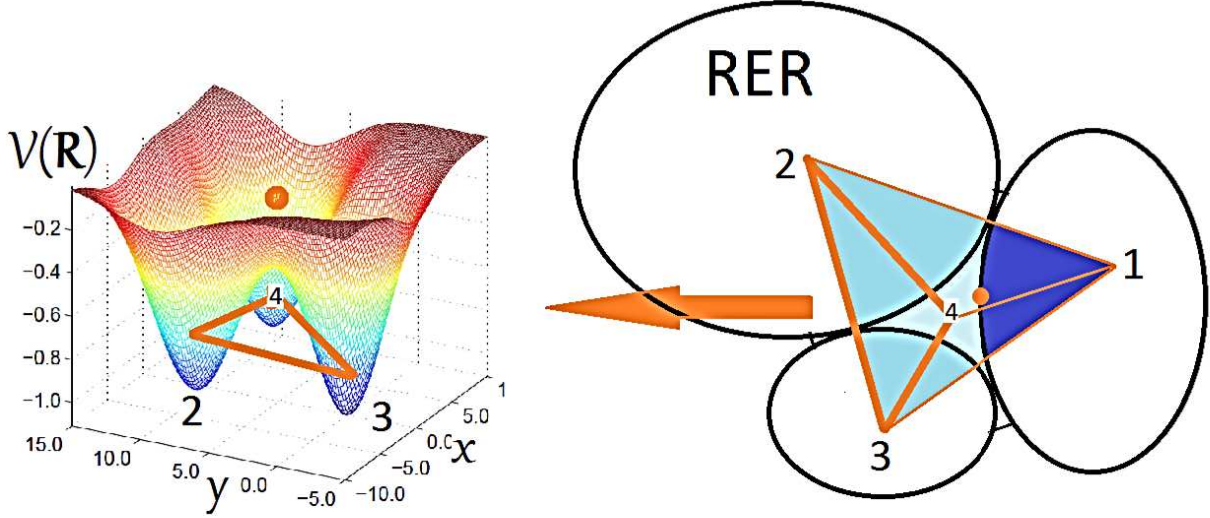


Figure 4: Origin of the tetrahedral void's effective triple-welled potential. Right panel: charged ions (probably  $O^-$  dangling bonds) adsorb on the RER surfaces delimiting a given void. One can consider the large ensemble of ions on the relevant surface of one RER (say n.1, deep blue) as replaced by a quasi-particle (orange dot) interacting with the complex distribution of all other ions (in the melt inside the void and on the other three RER surfaces, light blue coverage) in the narrow void's space. As a result, right panel: quasi-particle n.1 experiences an effective three-well potential  $V(\mathbf{R})$  from RER ns. 2-3-4 ( $\mathbf{R} = (x, y)$  is some coordinate in the plane of the 2-3-4-triangle and the height  $z$  is fixed). The same applies for the effective particles on RER ns. 2, 3 and 4 which experience, for pure topological reasons, also a three-well potential from the opposite triplets of RER.

which corrects the  $1/B$  prefactor into  $(1 - \frac{1}{54}(B/B^*)^2)/B$  when averaging over ATS triangular path's geometrical orientation is carried out.

More details in a future publication. However, we anticipate here the unusual temperature behaviour of this formula in the weak field limit, which completes the Curie formula, for the susceptibility  $\chi_{intr}^{tunn}$  due to the contribution to the bulk magnetisation  $M$  coming from the ATS in the “voids” between the jammed RER. Since the effective-TLS approximation for the magnetic ATS is applicable, we get in the end:

$$\chi_{intr}^{tunn}(T) = \frac{2}{3}\pi^3 \frac{n_{ATS}P^*}{\phi_0^2} \left(\frac{Q}{e}\right)^2 S_{\Delta}^2 (D_{0max}^2 - D_{0min}^2) \int_{D_{min}}^{\infty} \frac{dE}{E^2} \tanh\left(\frac{E}{2k_B T}\right) \quad (12)$$

and this is not quite Curie's law. In fact, working out the limits we have:

$$\begin{aligned} \lim_{T \gg D_{min}/k_B T} \chi_{intr}^{tunn}(T) &= \chi_{intr}^{tunn}(T) = \frac{2}{6}\pi^3 \frac{n_{ATS}P^*}{\phi_0^2} \left(\frac{Q}{e}\right)^2 S_{\Delta}^2 (D_{0max}^2 - D_{0min}^2) \frac{1}{k_B T} \\ \lim_{T \ll D_{min}/k_B T} \chi_{intr}^{tunn}(T) &= \chi_{intr}^{tunn}(T) = \frac{2}{3}\pi^3 \frac{n_{ATS}P^*}{\phi_0^2} \left(\frac{Q}{e}\right)^2 S_{\Delta}^2 (D_{0max}^2 - D_{0min}^2) \frac{1}{D_{min}} \end{aligned} \quad (13)$$

so that at  $T = 0$  this becomes a constant, while at slightly higher temperatures a fake Curie-law type term is recovered. This is part of the novel behaviour at high values of  $1/T$ . In the next Sections we shall see that, indeed, the data for  $M$  at weak fields do show deviations from the  $1/T$  Curie law precisely as indicated by Eq. (13). The fitting formula for the susceptibility of a piece of glass then becomes of the form:

$$\chi = -\chi_L + \frac{C}{T} + G \int_{D_{min}}^{\infty} \frac{dE}{E^2} \tanh\left(\frac{E}{2k_B T}\right) \quad (14)$$

where  $\chi_L$  is the closed-shells' Larmor contribution,  $C \propto n(\text{Fe})$  is the Curie constant and  $G \propto n_{ATS}$  is the new constant due to the collective coherent tunneling currents in the glass structure. More about the use of these formulas in Section D.

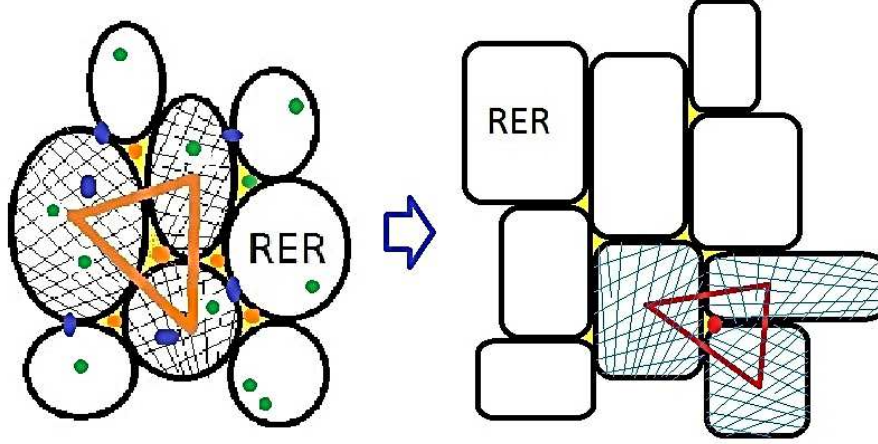


Figure 5: Compactification upon cooling of the RER close-packed arrangement (going from  $T \simeq T_g$ , left, to  $T \rightarrow 0$ , right hand side). The RER grow at the lowest temperatures at the expense of the material in the void, increasing at the same time the area of the RER-RER interfaces. Defects, in going from l.h.s to r.h.s., have been removed.

The last important ingredient for this theory is the substantial  $T$ -dependence that was found for  $N_{tunn}$ , the number of atomic-scale TS that make up, collectively, a single ATS quasi-particle described above. This crucial quantity clearly enters into the ATS renormalized tunneling parameters [18, 20]: the effective charge  $Q = N_{tunn}e$ , the flux-threaded surface  $S_{\Delta} \propto N_{tunn}a_0^2$  ( $a_0$  is of the order of Bohr's radius, see also below) and also the tunneling amplitude  $D_0 \propto N_{tunn}\Delta_{0min}$  and energy gap's cutoff  $D_{min} \propto N_{tunn}\Delta_{min}$  ( $\Delta_{0min}$  and  $\Delta_{min}$  being the atomic 2LS's STM cutoffs) [18, 28]. This state of affairs is responsible for the large ATS cutoffs-combinations values always found in data-fitting the ETM to available experimental data (a situation fully confirmed in this work, see Tables 3 and 4). The temperature-dependence of  $N_{tunn}$  arises from the shrinking of the RER tetrahedral void space upon deep cooling, when the RER walls grow at the expense of the surviving melt material in the voids, extending the RER-RER interfacial area and creating a tight cellular structure as shown in Fig. 5. This dependence can be written down, on general thermodynamics grounds, in the form

$$N_{tunn}(T) = N_0 \exp\left\{-\frac{\Delta\mu}{k_B T}\right\} \quad (15)$$

where  $\Delta\mu = \mu_{melt} - \mu_{RER}$  is the chemical potential difference between the active melt in the void and the RER surface. We will use this expression because it introduces one fit parameter less. However, a more precise non-equilibrium evaluation can be made by considering the RER surface growth, by activated deposition of melt species from the void's space (which shrinks when temperature decreases). Then one gets:

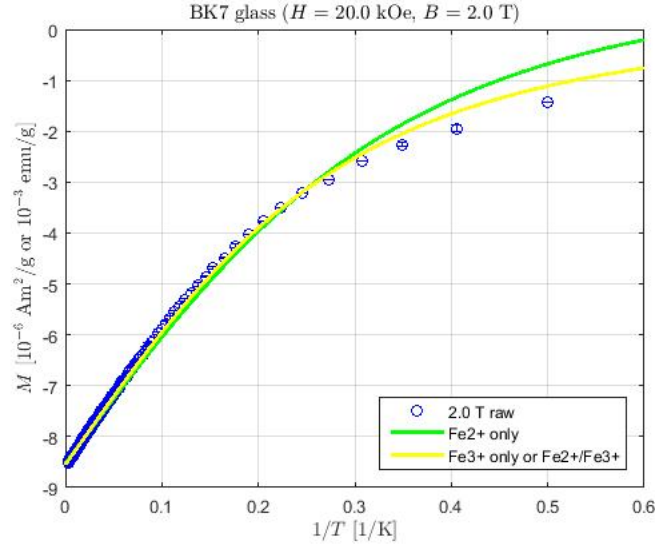
$$N_{tunn}(T) = N_0 \left(1 - \Gamma \exp\left\{\frac{E_0}{k_B T}\right\}\right) \quad (16)$$

where  $E_0$  is an activation energy and  $\Gamma$  a geometric parameter. As it turns out, both expressions (15) and (16) give very similar fitting values for  $\Delta\mu$  and  $E_0$  and same behaviour for  $N_{tunn}/N_0$  down to the range of  $T$  where new, unexpected phenomena appear. The expression Eq. (15) then allows to relate the ETM best-fit parameters to a reference temperature ( $T_0=1.26$  K, due to alternative knowledge of the parameters from  $C_p$  fits in that range [27]).

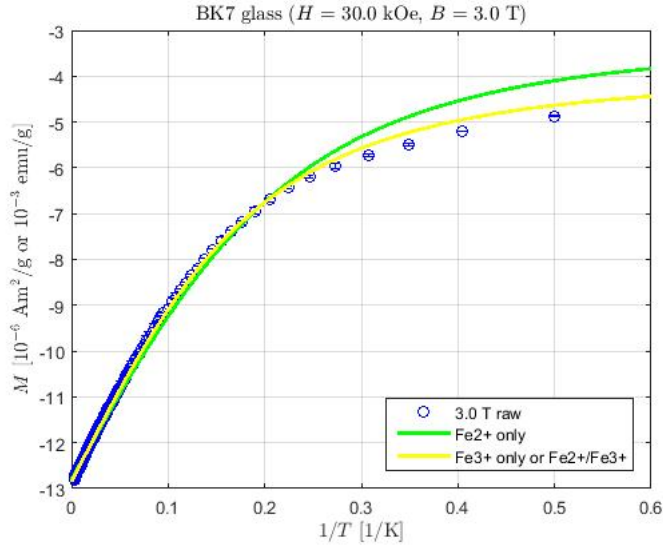
### C. Some More Data Fitting Results.

**C1) BK7 glass.** Fig. 6 reports two typical fit attempts with the LL-formula (Eq. (1) in the PA) for our SQUID-magnetisation data from a BK7-glass chip sample, much in the spirit of Fig. 1 in the PA (which was

for Duran). It is apparent that the LL form does not fit the data that well also for BK7 and especially at low  $T$ , moreover it induces the wrong conclusion that the sample contains only  $\text{Fe}^{3+}$  (which is false). The contribution unaccounted for comes from the intrinsic magnetisation  $M_{intr}^{tunn}(T, H)$  discussed in the previous Section B.



(a)



(b)

Figure 6: (a) BK7 glass sample's measurement of the magnetisation  $M$  at  $H=20.0$  kOe (2.0 T) in a SQUID-magnetometer. Raw data (black dots, with errorbars) being best fitted with Eq. (1) in the PA, so with one paramagnetic species, or two (in which case the  $\text{Fe}^{3+}$ -only scenario is always selected. (b) Same as in (a), but for  $H=30.0$  kOe (3.0 T).

Tables 1 and 2 (which we reproduce here from the PA for convenience's sake) as well as Fig. 7 show for BK7-glass how important the fluctuations are in both  $n(\text{Fe})$  and  $\chi_L$  by SQUID-scanning in  $T$  or  $H$  while keeping  $H$  or  $T$  constant, respectively, and employing the LL-fit form, Eq. (1) in the PA, alone. In Fig. 7 only the dependence of the putative  $n(\text{Fe}^{2+})$  is shown since mostly  $\text{Fe}^{2+}$  is expected (and found, in the proposed theory) and because the  $H$ -dependence of the missing contribution ( $\Delta n = n_{put}(\text{Fe}^{2+}) - n_{MS}(\text{Fe})$ ) coming from the glass is very reminiscent of other magnetic-field effects in glasses [12].

In Figs 8 and 9 the SQUID-runs that were collected for BK7 are reported, for fixed  $H$  and  $T$  respectively,

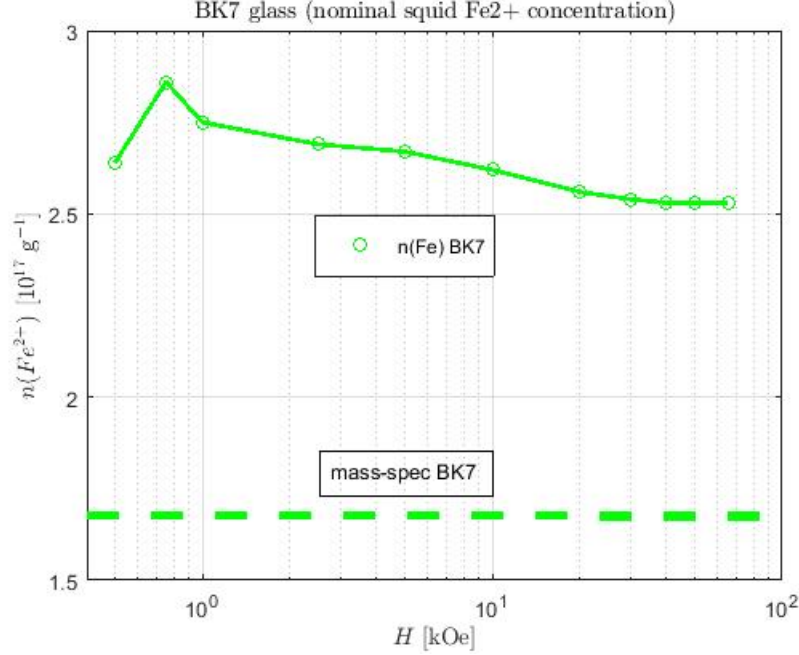


Figure 7: The dependence of the  $\text{Fe}^{2+}$  concentration extracted from SQUID-runs  $M$  vs.  $T$  and as a function of  $H$ . The shape of the "intrinsic"  $\Delta n = n(\text{Fe}^{2+}) - n_{MS}$  curve is very reminiscent of other magnetic effects in glasses [12] with a sharp maximum at low  $H$  followed by a slow decrease. The dashed line is the  $n_{MS}(\text{Fe})$  mass-spec value for Fe in BK7.

with the best fits of the data using  $M(T, H) = M_{LL}(H/T) + M_{intr}^{tunn}(T, H)$  as described in the previous Section of these SI ( $M_{LL}(H/T)$  as given by Eq. (1) in the PA).

The material and ETM parameters extracted from the best fit to the raw data are reported in Table 3 for SQUID-runs in fixed magnetic field.

They are to be compared with the parameters in Table 4 for SQUID-runs at fixed temperature.

Looking at these extracted parameters, Tables 3 and 4, the following immediate conclusions can be drawn:

- (a) The extracted total-Fe concentrations are in excellent agreement with the value extracted from mass-spectrometry; the small discrepancy (Table 3) can be attributed to the presence of minority paramagnetic Ti- and Cr-species in BK7 that have been lumped into Fe-only Langevin terms (the purpose is here to show that theory can also predict Fe-concentrations from SQUID runs as accurate as mass-spec's while keeping the number of fit-parameters low). The tiny discrepancy (if any) between the fixed- $H$  value of  $\chi_L$  and the fixed- $T$  value remains however unexplained. (b) Although the 2000 BK7 sample was much cleaner in Fe-contents, the ratio  $\text{Fe}^{2+}/\text{Fe}^{3+}$  ( $\approx 1.93$  for our sample, 1.97 for the 2000 sample) remains the same: BK7 has  $\approx 66\%$

Magnetic Field (kOe)	1.0	2.5	5.0	10.0	20.0	30.0	40.0	50.0	65.0	mass-spec
BK7 LL-parameters										
$n(\text{Fe}^{3+})$ $10^{17} \text{ g}^{-1}$	1.888	1.849	1.845	1.849	1.867	1.888	1.906	1.914	1.931	$1.657 \pm 0.019$
$\chi_L$ $10^{-7} \text{ emu/gOe}$	3.922	4.064	4.139	4.257	4.277	4.283	4.295	4.294	4.297	-
$n(\text{Fe}^{2+})$ $10^{17} \text{ g}^{-1}$	2.752	2.690	2.667	2.621	2.559	2.541	2.536	2.526	2.526	$1.657 \pm 0.019$
$\chi_L$ $10^{-7} \text{ emu/gOe}$	3.922	4.064	4.136	4.249	4.262	4.266	4.277	4.276	4.278	-

Table 1: LL-fitting (Eq. (1) in PA) parameters extracted from different SQUID runs of  $M$  vs.  $1/T$  at stated  $H$ -values for a BK7-prism chip having mass 96.8 mg. The first row is obtained from best fits when both  $\text{Fe}^{3+}$  and  $\text{Fe}^{2+}$  species are allowed (in practice one always obtains  $n(\text{Fe}^{2+})=0$ ); for comparison, the results when  $\text{Fe}^{2+}$ -only is allowed are shown in the second row. The precise mass-spec value of  $n(\text{Fe})$  is also indicated (errorbar was estimated from spectrometer specifications, repeating the analysis and by dissolving separate BK7-prism chips, including this one).

Temperature (K)	2.0	4.5	7.5	10.0	20.0	mass-spec
BK7 LL-parameters						
$n(\text{Fe}^{3+}) 10^{17} \text{ g}^{-1}$	1.746	1.877	1.969	2.035	3.135	$1.657 \pm 0.019$
$\chi_L 10^{-7} \text{ emu/gOe}$	4.178	4.269	4.326	4.350	4.686	-
$n(\text{Fe}^{2+}) 10^{17} \text{ g}^{-1}$	2.414	2.905	3.358	3.681	6.206	$1.657 \pm 0.019$
$\chi_L 10^{-7} \text{ emu/gOe}$	4.178	4.269	4.326	4.350	4.686	-

Table 2: The same as in Table 1, but as extracted from SQUID-runs of  $M$  vs.  $H$  at stated  $T$ -values.

Constant- $H$ parameters	BK7 glass this sample	mass-spec this sample	BK7 glass 2000 sample [32, 27]
$n(\text{Fe}^{2+}) 10^{17} \text{ g}^{-1}$	$1.099 \pm 0.001$		0.067
$n(\text{Fe}^{3+}) 10^{17} \text{ g}^{-1}$	$0.599 \pm 0.001$		0.034
$n_{tot}(\text{Fe}) 10^{17} \text{ g}^{-1}$	$1.698 \pm 0.001$	$1.657 \pm 0.019$	0.101
$\chi_L 10^{-7} \text{ emu/gOe}$	$4.227 \pm 0.095$		3.600
$n_{ATS} 10^{16} \text{ g}^{-1}$	$1.352 \pm 0.001$		1.400
$D_{min} 10^{-2} \text{ K}$	$2.671 \pm 0.076$		5.990
$D_{0min} \frac{Q}{e} S_{\Delta} 10^5 \text{ K}\text{\AA}^2$	$2.717 \pm 0.310$		0.887
$D_{0max} \frac{Q}{e} S_{\Delta} 10^5 \text{ K}\text{\AA}^2$	$2.925 \pm 0.297$		1.200
$\Delta\mu \text{ K}$	$0.319 \pm 0.067$		0.480

Table 3: Table of parameters extracted from best-fitting with  $M = M_{LL} + M_{intr}^{tunn}$  (Eq. (1) in the PA and Eq. (10)) our  $M$  vs.  $T$  SQUID-runs gathered in Fig. (8). The set on the left-hand-side is for our own BK7 sample chip (96.8 mg mass), while the set of parameters on the right is for the best-fit [27] to SQUID-magnetisation data published in [32] for yet another BK7 sample in  $H=30.0$  kOe (mass and mass-spec analysis unknown).

Constant- $T$ parameters	BK7 glass this sample	mass-spec this sample	BK7 glass 2000 sample [32, 27]
$n(\text{Fe}^{2+}) 10^{17} \text{ g}^{-1}$	$1.098 \pm 0.001$		0.067
$n(\text{Fe}^{3+}) 10^{17} \text{ g}^{-1}$	$0.569 \pm 0.001$		0.034
$n_{tot}(\text{Fe}) 10^{17} \text{ g}^{-1}$	$1.667 \pm 0.001$	$1.657 \pm 0.019$	0.101
$\chi_L 10^{-7} \text{ emu/gOe}$	$4.137 \pm 0.004$		3.600
$n_{ATS} 10^{16} \text{ g}^{-1}$	$1.340 \pm 0.001$		1.400
$D_{min} 10^{-2} \text{ K}$	$5.238 \pm 0.488$		5.990
$D_{0min} \frac{Q}{e} S_{\Delta} 10^5 \text{ K}\text{\AA}^2$	$2.107 \pm 0.032$		0.887
$D_{0max} \frac{Q}{e} S_{\Delta} 10^5 \text{ K}\text{\AA}^2$	$2.160 \pm 0.033$		1.200
$\Delta\mu \text{ K}$	$0.615 \pm 0.615$		0.480

Table 4: The same as in Table 3, but for our  $M$  vs.  $H$  SQUID-runs gathered in Fig. (9). The set on the left-hand-side is for our own BK7 sample chip (96.8 mg mass), while the set of parameters on the right is, for the sake of comparison, for the best-fit [27] to SQUID-magnetisation data ( $M$  vs.  $T$  at  $H=30.0$  kOe) published in [32] for yet another BK7 sample (mass and mass-spec analysis unknown).

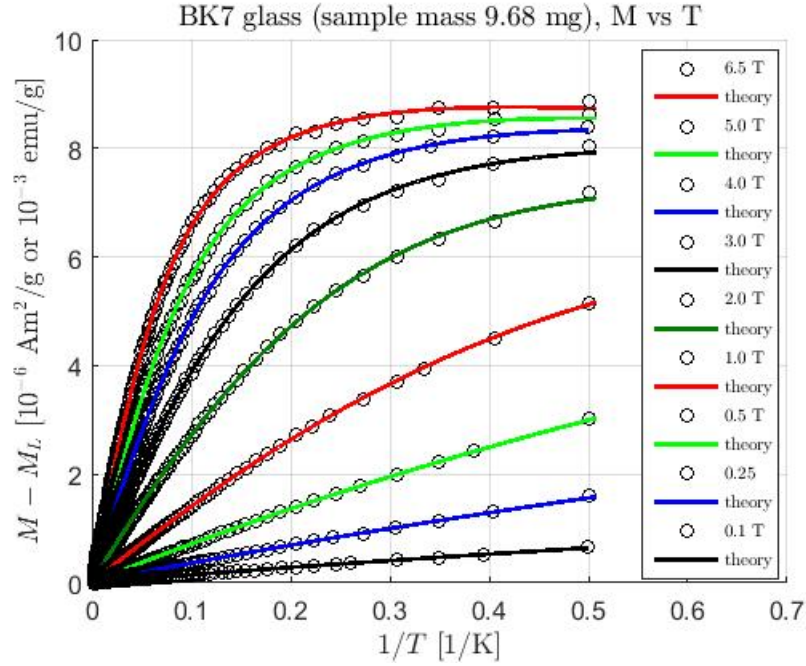


Figure 8: The original SQUID data  $M$  vs.  $1/T$  (after shifting the raw data by a constant  $M_L = -\chi_L H$  term with  $\chi_L$  as given in the Table 3 below) and their best fit to the ETM-theory. The best-fitting procedure has been always applied to the raw data.

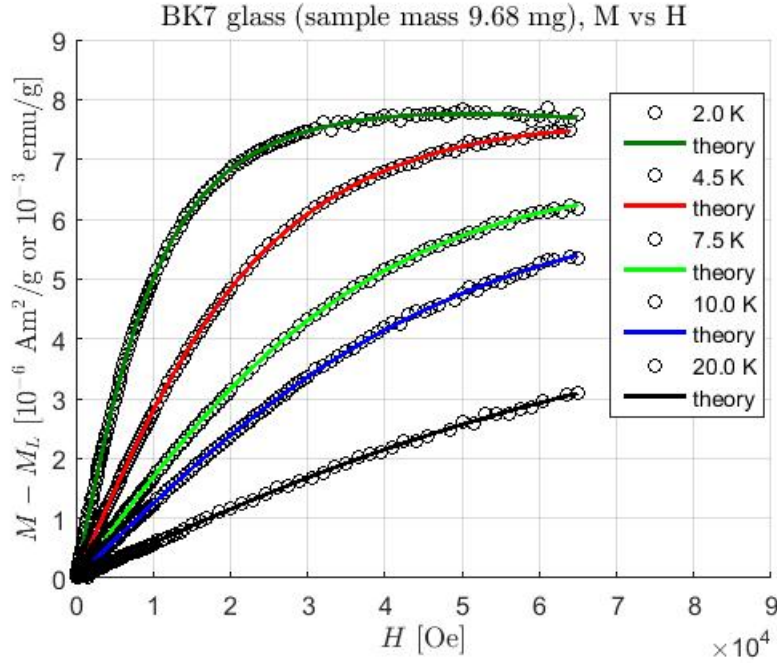
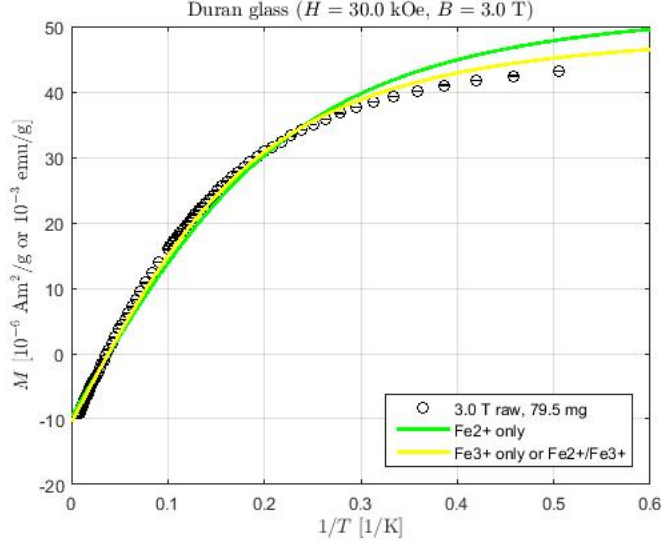


Figure 9: The original SQUID data  $M$  vs.  $H$  (after shifting the raw data by a  $M_L = -\chi_L H$  term with  $\chi_L$  as given in the Table 4 below) and their best fit to the ETM-theory. The best fit was applied to the raw data.

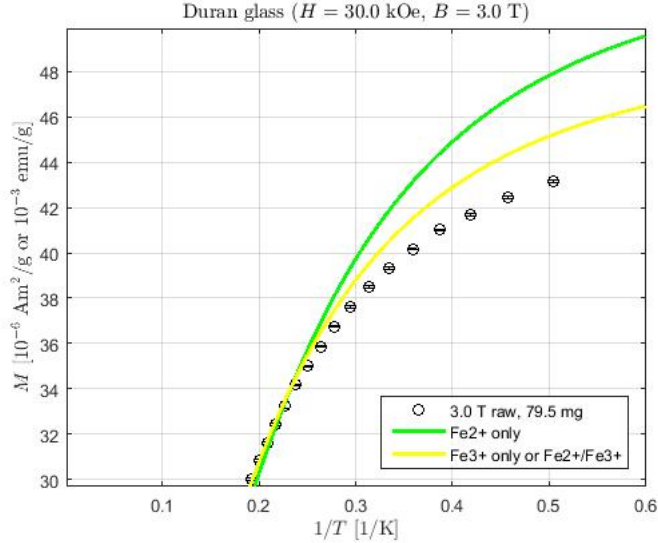
$\text{Fe}^{2+}$  and 33%  $\text{Fe}^{3+}$  and this seems to be linked to oxide-composition. (c) Likewise for the concentration of ATS, that appears to be the same in both samples; we expect, however, that  $n_{ATS}$  is also strongly linked to cooling-rate and other vetrification conditions and the size  $2\xi$  of BK7's RER remains the same as for the

2000 sample,  $\approx 62$  nm. (d) The other best-fit parameters for the ETM remain only of the same order of magnitude for the two BK7 samples: the ETM is, after all, just an effective theory and can be improved.

**C2) Duran and BAS glasses.** In Figs. 10 and 11 we report the raw data and naive LL SQUID-magnetisation theory fits for the Duran shards we examined and for  $H=30.0$  kOe (3.0 T) and 50.0 kOe (5.0 T) (caution: different samples). It is clear (especially from the details at low  $T$ ) that a new (albeit small) contribution is absent in the fitting theoretical expression.



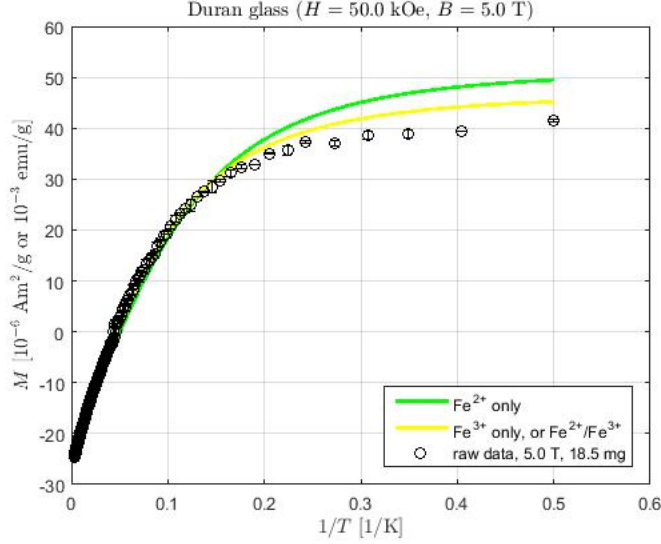
(a)



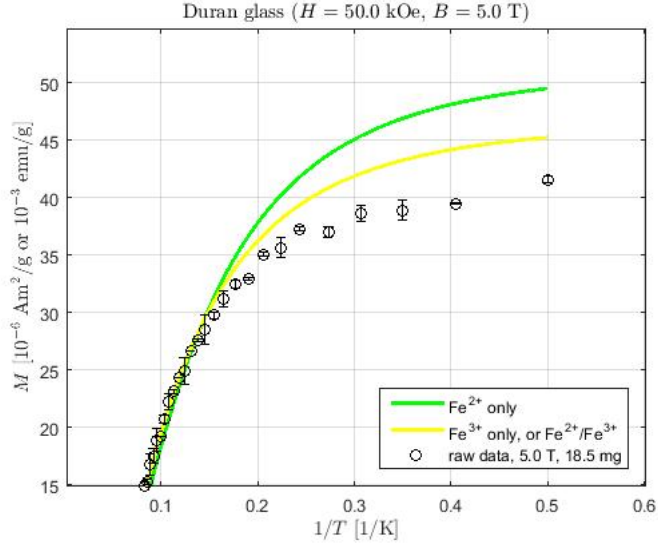
(b)

Figure 10: (a) Duran 79.5 mg, 30.0 kOe (3.0 T) raw data fitted with the LL form Eq. (1) in the PA. (b) Same as (a), but for the lowest temperatures in an expanded vertical scale, to show the strong deviation between naive LL theory and the data.

In Figs. 12 and 13 we report the raw data and naive LL SQUID-magnetisation theory fits for the BAS-glass fragments we examined and for  $H=30.0$  kOe (3.0 T) and 50.0 kOe (5.0 T). Again, although the Fe-content is much higher, it is clear (especially from the details at low  $T$ ) that a new (albeit small) contribution is absent in the fitting theoretical expression.



(a)



(b)

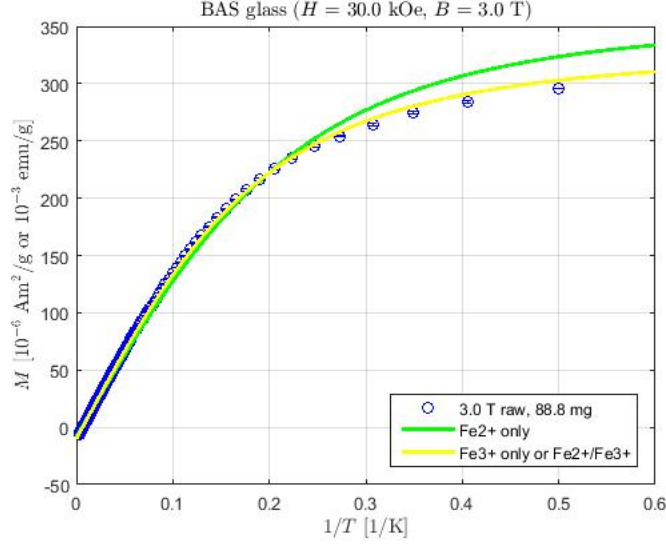
Figure 11: (a) Duran 18.5 mg, 50.0 kOe (5.0 T) raw data fitted with the LL form Eq. (1) in the PA and as already reported in Fig. 1 of the PA. (b) Same as (a), but for the lowest temperatures in an expanded vertical scale, to show the strong deviation between naive LL theory and the data.

In Figs 14 and 15 we report the universality tests for  $M - M_L$  as a function of  $H/T$  for these other two multi-silicate glasses that we have studied. Again, we subtracted the Larmor contribution  $-\chi_L H$  as determined from the naive  $M_{LL}$  fit from Eq. (1) in the PA. Clearly, universality does not hold.

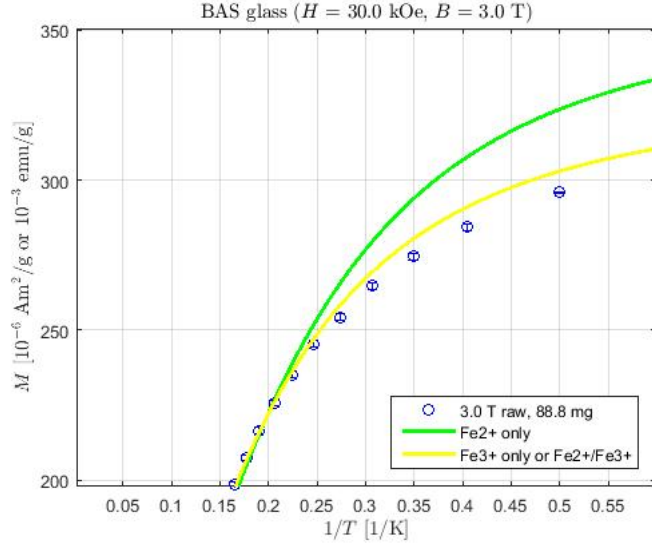
We now report, for the Duran and BAS glasses, the qualitative MS analysis for the Fe-group elements. Again, Fe is the predominant element and the others are present in such smaller concentration and have the wrong  $J_s$  value to affect our conclusions.

For comparison, we report in Table 7 the results already presented in the PA of the qualitative MS analysis for the BK7 glass samples that were studied in the SQUID magnetometer.

More data and data analyses for the SQUID measurements on the Duran- and BAS-glasses will be presented elsewhere [33]. Here we conclude by presenting two further studies of the effect of subtracting fixed fractions  $x$  of  $\text{Fe}^{2+}$  and  $1 - x$  of  $\text{Fe}^{3+}$  Langevin contributions from the raw data for  $M - M_L$  (the latter  $M_L$  as determined from naive  $M_{LL}$  best-fits). What remains is not only non-zero, but indicates that it presents the



(a)



(b)

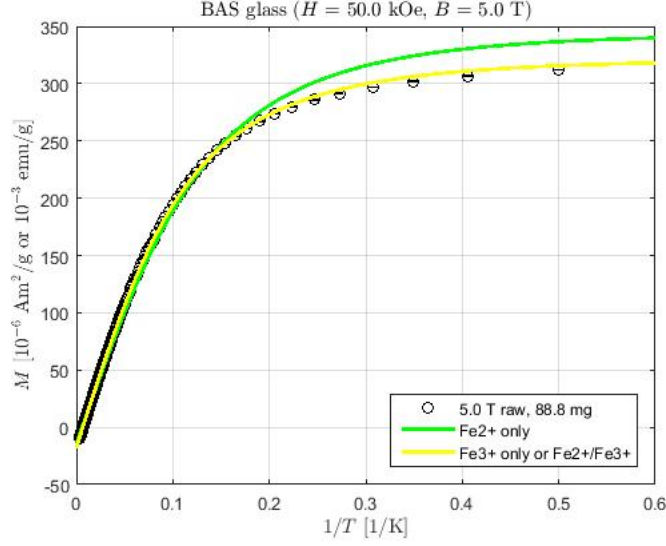
Figure 12: (a) BASw 88.8 mg, 30.0 kOe (3.0 T) raw data fitted with the LL form Eq. (1) in the PA. (b) Same as (a), but for the lowest temperatures in an expanded vertical scale, to show the strong deviation between naive LL theory and the data.

Fe	Ti	V	Cr	Mn	Co	Ni	Cu
1	0	0.005	0.017	0.023	0.002	0.004	0.008

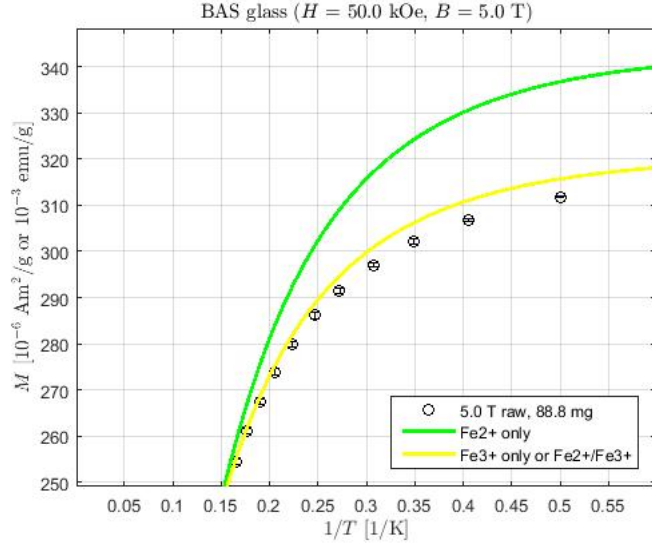
Table 5: Relative concentration (taking  $n(\text{Fe})=1$ ) of all other Fe-group magnetic elements present in similar Duran-glass shards as those SQUID-characterised in this work and from our own qualitative MS analysis.

odd shape as a function of either  $1/T$  or  $H$  as predicted by the ETM theory and practically for any value of  $x$ . In Fig. 16 for Duran- at a temperature of 2.2 K kOe and in Fig. 17 for BAS-glass in a field of 30.0 kOe (3.0 T) we see that the application of the ETM theory singles out the right (MS-ascertained) values of  $x$  for both Duran- and BAS-glass and give good fits to the modified experimental data.

In order to clearly state the case for glass paramagnetism, in Fig. 18(a) we show the raw magnetisation



(a)



(b)

Figure 13: (a) BASw 88.8 mg, 50.0 kOe (5.0 T) raw data fitted with the LL form Eq. (1) in the PA and as already reported in Fig. 1 of the PA. (b) Same as (a), but for the lowest temperatures in an expanded vertical scale, to show the strong deviation between naive LL theory and the data.

Fe	Ti	V	Cr	Mn	Co	Ni	Cu
1	0	0.001	0.011	0.005	0	0.005	0.023

Table 6: Same as previous Table 5, but for BAS-glass calcinated paste scrapings.

Fe	Ti	V	Cr	Mn	Co	Ni	Cu
1	0.1	0	0.1	0.01	0	0.01	0.01

Table 7: Same as previous Tables 5 and 6, but for the very same BK7-chips SQUID-characterised in this work.

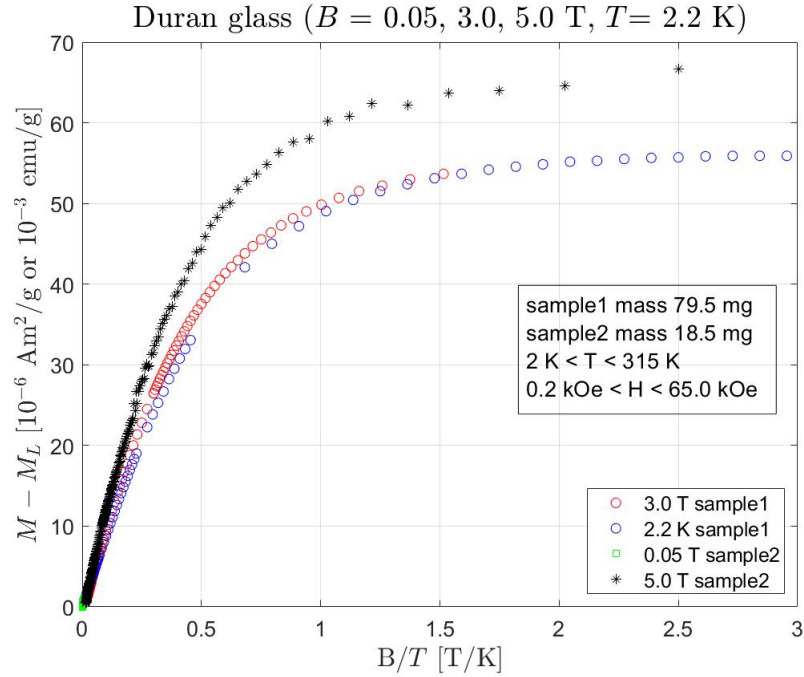


Figure 14: Universality test for our SQUID-run measurements on Duran glass (all what was available). The raw data have been re-plotted in the same spirit as for Fig. 2 in the PA. As always,  $B = \mu_0 H$ .

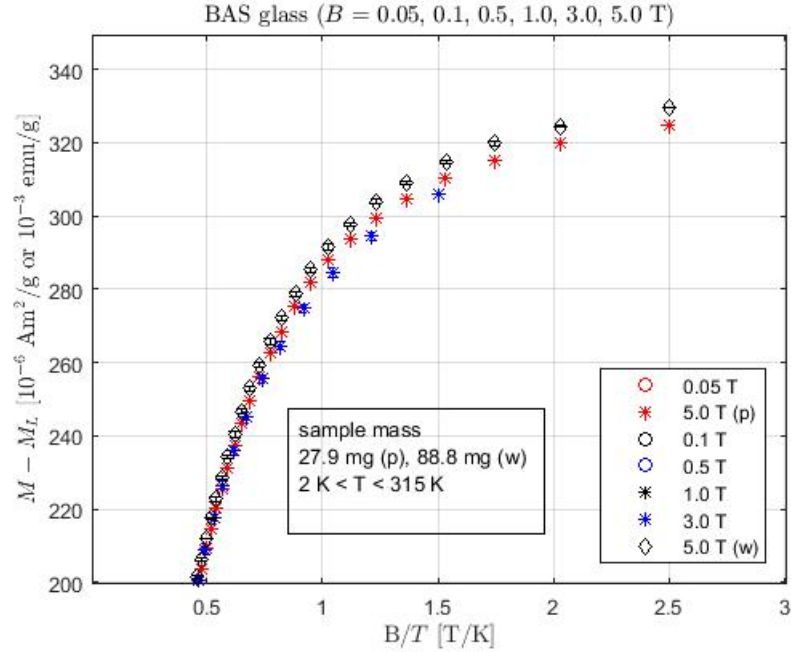


Figure 15: Universality test for our SQUID-run measurements on BAS glass (for clarity, not all of our fixed- $H$  runs are reported). The raw data have been re-plotted in the same spirit as for Fig. 2 in the PA.  $B = \mu_0 H$ .

data for a case at fixed  $H$  (30.0 kOe or 3.0 T) along with the Larmor-Langevin contributions consistent with the MS-ascertained Fe-concentration and optimal Fe(2+)/Fe(3+) partitioning in a sample of BAS-w glass. The  $n(\text{Fe}^{2+})$  is from the theory best-fit (the value of  $\chi_L$  also), however any other partitioning would give a curve that cannot explain the data. The missing contribution is accounted for only by the ETM and is the

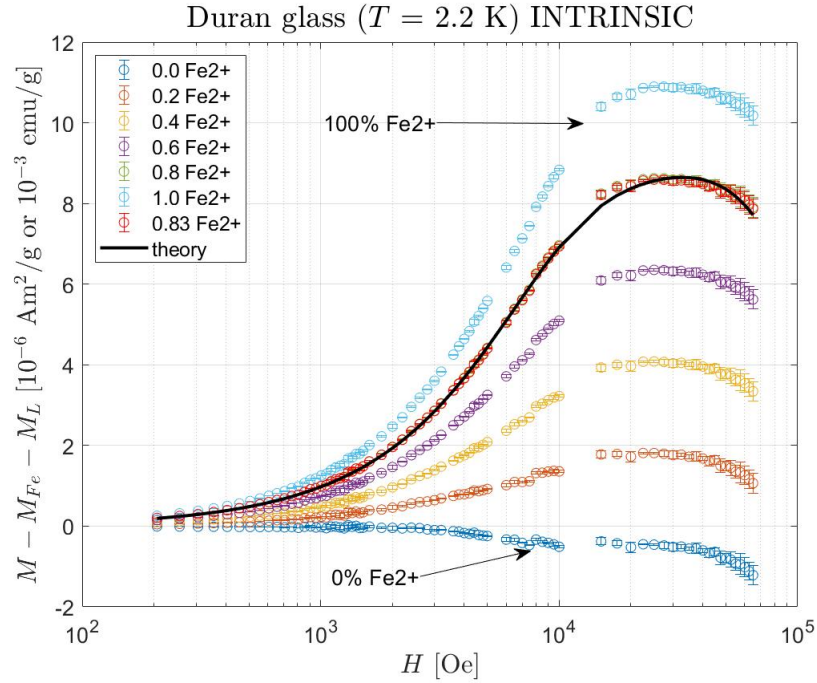


Figure 16: Re-plot of raw data for Duran glass after subtraction of the Langevin contribution from  $x n_{MS}(\text{Fe}) \text{Fe}^{2+}$ -ions and  $(1 - x) n_{MS}(\text{Fe}) \text{Fe}^{3+}$ -ions with  $n_{MS}(\text{Fe}) = 1.47 \times 10^{18} \text{ g}^{-1}$  the MS-ascertained value. The raw data have been re-plotted in the same spirit as for Fig. 4(a) in the PA. From top to bottom  $x = 1.0, 0.8, 0.6, 0.4, 0.2, 0.0$  and the ETM theory singles out the right concentration ratio.

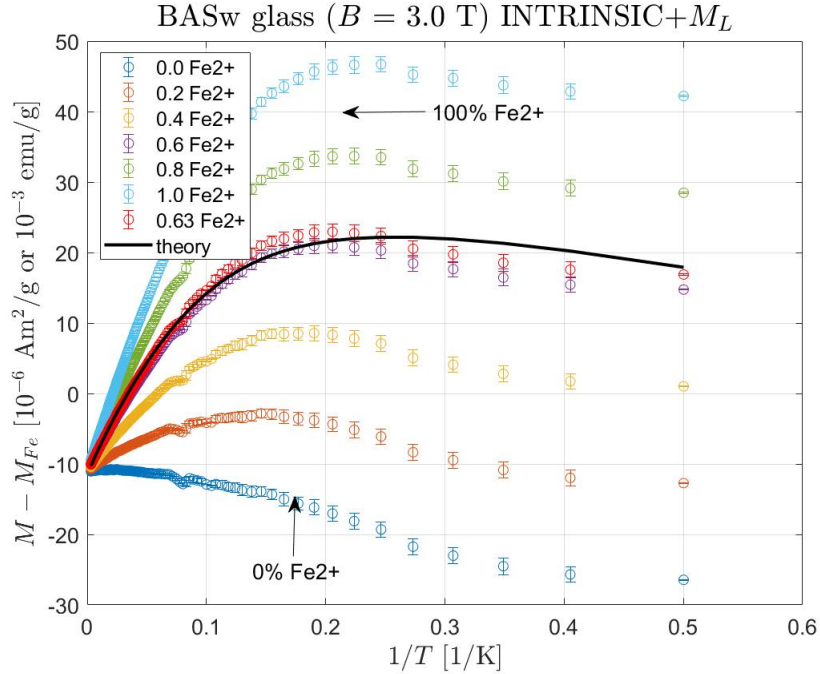


Figure 17: As for Fig. 16, but for BAS-w glass and with  $n_{MS}(\text{Fe}) = 7.13 \times 10^{18} \text{ g}^{-1}$  the MS-ascertained value of Fe-concentration. The raw data have been re-plotted in the same spirit as for Fig. 3(a) in the PA.

contribution from the ATS, also shown in the figure (Fig. 18(a)). The theoretical ATS curve clearly shows a broad peak as a function of  $1/T$  at the lowest temperatures. For the same sample and measurements,

in Fig. 18(b) we report the subtracted data points for the intrinsic  $M_{intr}$  part as a function of  $1/T$  and the theoretical ATS contribution for comparison. The theory fit is satisfactory, but new phenomena (yet unaccounted for by theory) appear at the lowest reached temperatures.

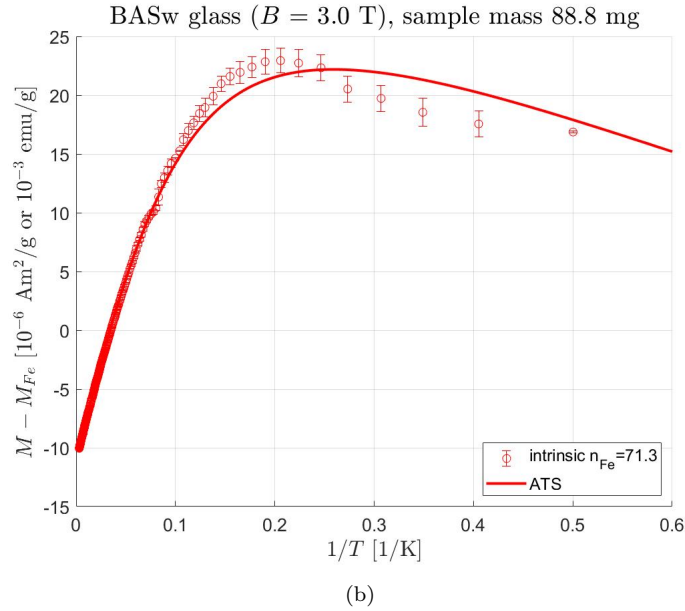
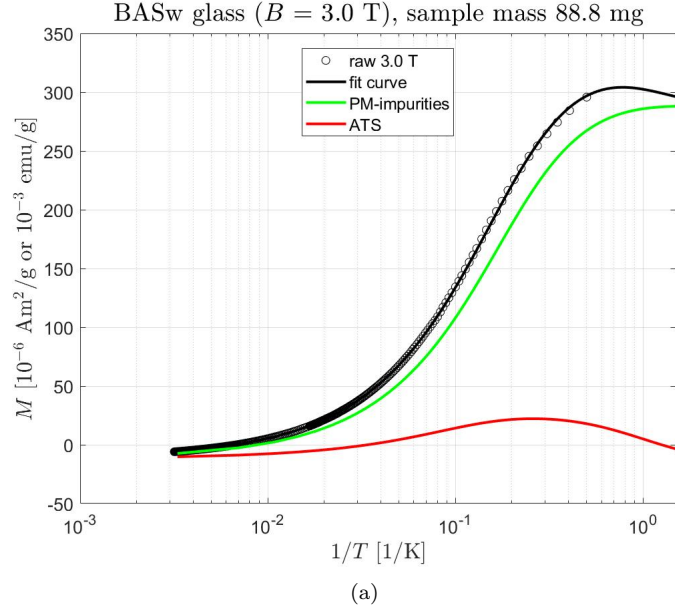


Figure 18: (a) BASw 88.8 mg, 30.0 kOe (3.0 T) raw data (black circles) fitted with the LL form Eq. (1) in the PA (green curve) where the Fe concentration is fixed at the MS-acertained value ( $71.3 \times 10^{17} \text{ g}^{-1}$ ). The Fe(2+)/Fe(3+) partition is fixed by the present theory ( $x=0.63$ ) but any other value of  $x$  gives worsening LL agreement with the data. The missing contribution is here indicated in red (from theory) and provides the full fit in black to the raw data. (b) Same as (a) for the missing contribution to the raw data, now as subtracted data points (red dots) with the LL contributions taken away. The red continuous curve is the same as in (a), the ETM theory's ATS contribution.

**D. Further Discussion about Curie Law and Comparison with ETM-Theory.** The experimental

data for the bulk magnetisation of point-like samples of the above-stated glassy systems have been analysed with the formula:

$$M(T, H) = -\chi_L H + M_{\text{Fe}}(H/T) + M_{intr}^{tunn}(H, T) \quad (17)$$

where the first (Larmor) and the second (Langevin) terms are those of Eq. (1) in the PA and the third is the ATS coherent-tunneling currents' ensuing magnetisation as discussed in Section B (briefly), Eq. (10), and in Ref. [27]. In the limit of weak magnetic fields  $H/T \rightarrow 0$  the second term and the third term assume the forms given in Eq. (14) for the susceptibility  $M/H$ . Here, we want to show how the form Eq. (14) (alternatively the full form containing Eq. (10)) can account for deviations from the Curie law. Fig. 19(a) for Duran- and (b) for BAS-glass show our weakest magnetic field ( $H=500.0$  Oe, or 0.05 T) bulk magnetisation data points, with the dashed blue line representing the Curie law. Not only this procedure extracts a faulty  $n(\text{Fe})$  concentration value, but also it does not provide a good fit at the lowest temperatures. The fit to the data by our theory (full black line) considerably improves agreement at all values of  $1/T$ , moreover it extracts the right concentration  $n(\text{Fe})$  and works out (green line) the correct Langevin contribution. The red line represents the contribution from the ATS coherent-tunneling currents.

These considerations suggest an elegant new test for the ETM-, magnetic ATS-theory presented in Section B. If the Larmor susceptibility  $\chi_L$  of the sample can be ascertained in an independent way, then measuring the magnetic susceptibility  $\chi$  as a function of very low temperatures  $T$  (below 4.0 K and at least down to 300 mK) will produce an interesting graph plotting  $T(\chi - \chi_L)$  vs.  $T$ . In an ordinary weakly Fe-doped insulating non-magnetic crystal this should produce a constant  $C$ , while from the expression in Eq. (14) we should have (note:  $\chi_L$  taken with its negative sign here):

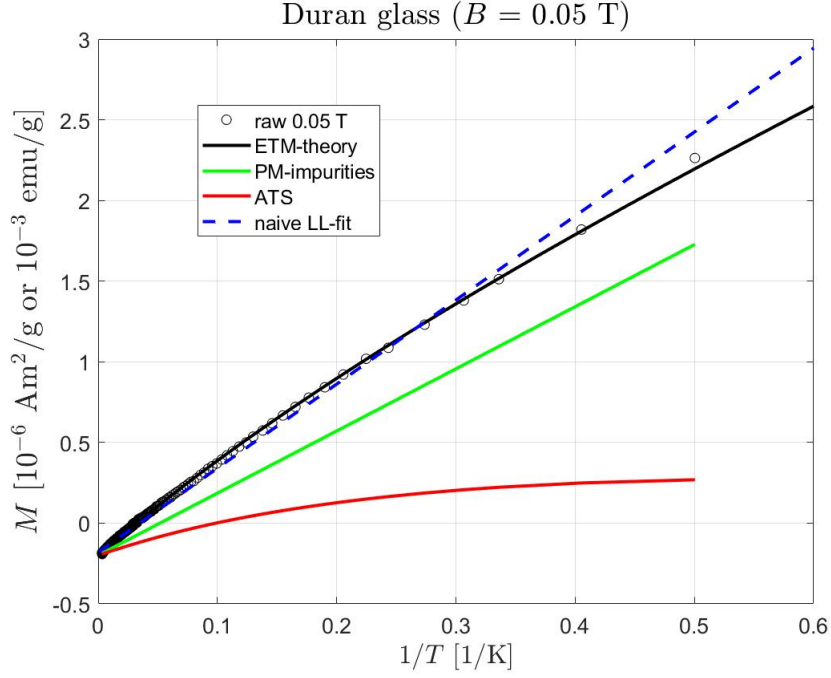
$$T(\chi - \chi_L) = C + GT \int_{D_{min}}^{\infty} \frac{dE}{E^2} \tanh\left(\frac{E}{2k_B T}\right) \quad (18)$$

and this should increase linearly like  $C + \frac{G}{D_{min}}T$  with temperature, with  $C \propto n(\text{Fe})$  the Curie constant (one for  $\text{Fe}^{2+}$  and one for  $\text{Fe}^{3+}$  in fact). A simple form that should be contrasted with a simple constant  $C$  for  $\lim_{T \rightarrow 0} T(\chi - \chi_L)$  in the case of the crystal.

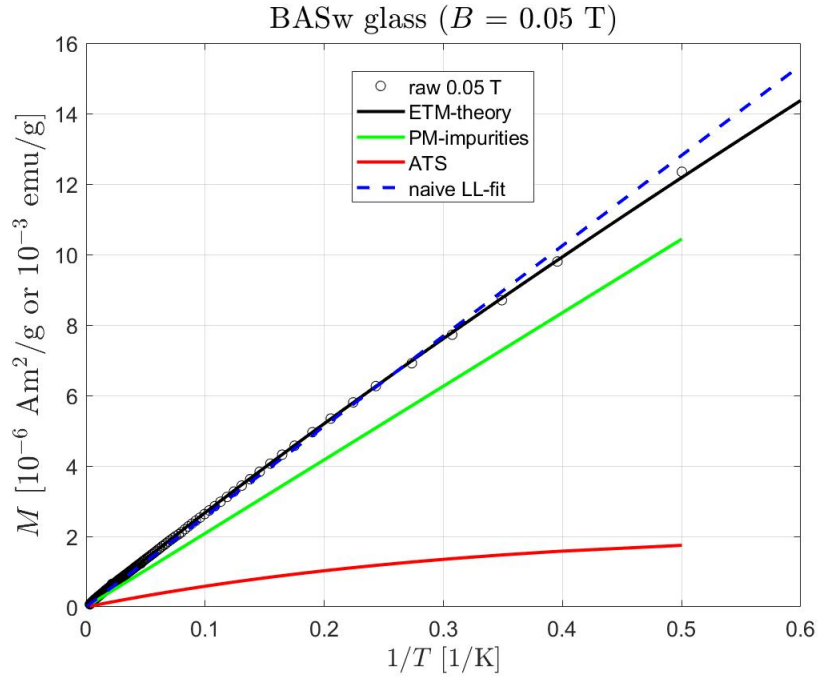
**E. The  $M_{intr}$  Temperature Oscillations and the High Field Limit.** Here we comment some more on the theoretical qualitative interpretation of the data, for all of the glasses. For the oscillations in the graph of  $M_{intr}$  vs.  $T$  (Fig. 6 in the PA) we offer a tentative but very compelling explanation. For a start, the oscillations can be observed also for the BAS-p magnetisation data, polished of the Larmor-Langevin contributions. In Fig. 20 we reproduce the data for  $M_{intr}$  at indicated conditions.

In order to provide a plausible theoretical explanation for these oscillations in  $M_{intr}$  we resort to the poly-cluster or cellular model of glass structure advocated for in this paper. We do have in fact some direct experimental evidence for the existence of such cells jammed against each other, obtained precisely for BAS glass with an expedient (seeding the hot glass-forming liquid with foreign particles of the appropriate size [34]) which produces order 100  $\mu\text{m}$  size cells visible with an ordinary microscope. Fig. 21 in particular shows the white cells under a microscope for one "black" BAS glass manufacture of some 10 mm width and 5 mm thickness. However for unseeded glass – or self-seeded, or highest- $T_m$  (melting point) component seeded glass – the size of these cells is estimated to be from O(1) to O(100) nm and then collective magnetic effects are expected.

To simulate this structure, and implement the magnetic-ATS model in Section B, consider the 2D cartoon situation depicted in Fig. 22(a) for some temperature  $T_1 < T_g$ : the intrinsic magnetisation is roughly proportional to the overall white-regions extension (per unit area or mass). In fact it is proportional to the overall white-regions inner perimeter length in 2D. Ignoring any slow-growth (or shrinking) of the oval RER size, let us change quasi-statically the temperature to a nearby value  $T_2$ , giving rise to the slightly different equilibrium configuration of Fig. 22(b). It seems natural to expect that the  $M_{intr}^{tunn}(T_2)$  will be only slightly different from (but not the same as)  $M_{intr}^{tunn}(T_1)$  and that that moving slightly in temperature the oval RER will rotate slightly giving rise to oscillations as a function of  $T$ . More details and calculations in coming publications, but heuristically this mechanism explains the  $M_{intr}(T)$  oscillations for fixed magnetic field  $H$ . Clearly, for a system of random-packed jammed spheres (or circles) all of the same size we do not expect any change of  $M_{intr}(T)$  for fixed  $H$  with changing temperature in this picture. Thus, the oscillations in the intrinsic magnetisation are evidence for the polydisperse size-distribution and non-spherical shape of the RER.



(a)



(b)

Figure 19: The failure of the Curie law in glasses. (a) Data for the magnetisation of a small shard of Duran-glass: The dashed blue line is the naive Curie law, which extracts the wrong value of the Fe-concentration (and all  $\text{Fe}^{3+}$ , which is false), the real Langevin contribution ( $\text{Fe}^{2+}$  and  $\text{Fe}^{3+}$ ) being the green line. While the red line is the contribution from the ATS coherent-tunneling currents, the black line is the full best fit. (b) Same as (a), but for a BAS-glass sample. Errorbars are about the same size of the dots.

Interestingly, there might be here a connection with the so-called "Boson-peak" phenomenology [35] as indeed the oscillations are at relatively high temperatures where the peak of the specific heat and of the vibrational

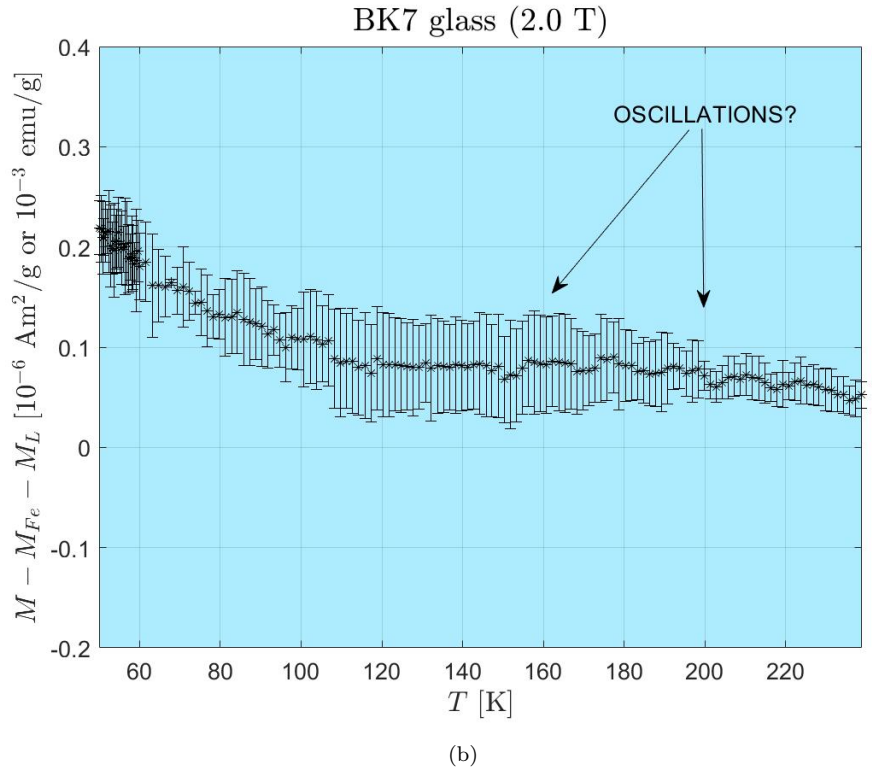
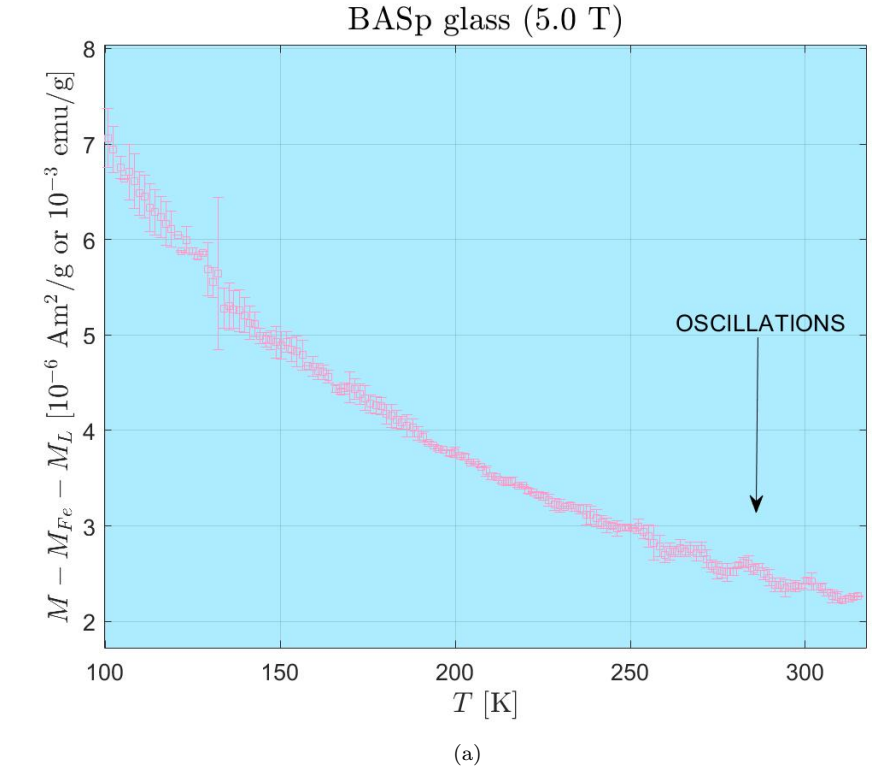


Figure 20: (a) BAS-p glass at 50.0 kOe (5.0 T) raw data after subtraction of the LL form (Eq. (1) in the PA) for MS/theory-fit extracted Fe-concentrations: distinct oscillations as a function of  $T$  are noted, almost as clear as for Duran glass (PA Fig. 6). (b) Same as (a) but for BK7 glass at 20.0 kOe (2.0 T): oscillations, if present, are much weaker for this type of glass, signalling that the RER size is largest for this glass.

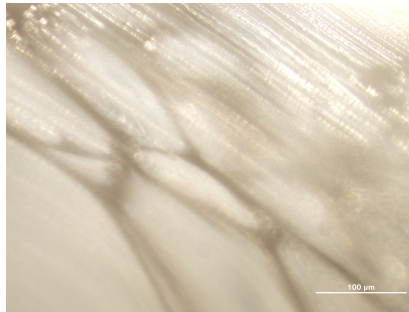


Figure 21: Ordinary optical microscopy image of the cell-structure of a manufacture of seeded BASb (black) glass [34], showing the jammed cells medium-range structure. Marked self-forming grooves on the clear manufact's surface are also visible.

spectrum  $g(\omega)/\omega^2$  ( $g(\omega)$  being the density of states at frequency  $\omega$ ) is observed. Then, as envisaged by one of us [36], the Boson-peak should arise from the vibration modes of the closed-packed, jammed non-spherical RER ensemble.

Incidentally, the dynamics of the single RER may be the correct explanation also for recent findings near  $T_g$  in a synchrotron-radiation XPCS experiment conducted on a sodium-silicate glass sample [37]. In such study below the nominal  $T_g$  faster than expected dynamics was observed with relaxation times typically in the 100 s range. An explanation might be offered by rotational diffusion of the compact but non-spherical RER. More in forthcoming publications.

Another important challenge in explaining the data with the present theory is the high-field values region. We fitted the data with the ETM theory discussed in detail in Section B, which strictly-speaking considers only two of the (at least) three energy levels of each single magnetic-sensitive ATS. This description is acceptable for intermediate  $H$  values, but by following the descent of the effective ETM-theory  $M_{intr}^{tunn}$  values one would arrive at the situation where a *negative* (thus diamagnetic) magnetisation occurs. This is indeed not realistic, and an improved high- $H$  theory (taking all three levels of Hamiltonian (4) into account) shows that at high magnetic field the  $M_{intr}^{tunn}$  calculated magnetisation smooths away to a slow descent with increasing high values of  $H$  [38]. In Fig. 23 we present the situation for the BK7 glass at  $T=4.5$  K, where the raw data are for the magnetisation after subtraction of the appropriate (MS determined Fe-concentration and best fits) Larmor and Langevin contributions. Both the low- and intermediate-magnetic field predicted  $M_{intr}^{tunn}$  and the high-field  $M_{intr}^{tunn}$  curves are drawn from the present theoretical treatment and the match is satisfactory, certifying that the intrinsic magnetisation is expected to fall off gently with increasing high fields.

### E. Novel Quantum-Coherence Phenomena.

We finally comment on the very low- $T$  behaviour of  $M_{intr}$ . Very few data points for  $M_{intr}$  are available at such temperatures, but for BAS glass Fig. 5(a) (in the PA) already indicates interesting deviations below 4 K from the theoretical curve here obtained. While for BK7 glass, the last experimental data point in Fig. 3 (in the PA) at the lowest available temperature of 2 K might be off the present theory's curve because something new takes place for  $T < 3$  K. What could the new physics be?

Elaborating further on what stated in the PA, in reality evidence from the last 10 years or so of study of the ETM applied to low-temperature data in mixed glasses suggests that the TLS in glasses sit at the interface between the solid-like RER and the fluid-like particles contained in their random-packing's "voids" [18, 39]. A better hypothesis is that, in fact, the TLS hide at the RER-RER interfaces and are precisely the degrees of freedom keeping the polycluster or cellular structure together when the same-polarisation charged chemical species in the "voids" would tend to make the polycluster structure fly apart. Within this scenario, then glasses are then truly frustrated systems (in a similar, but different sense as spin-glasses are [40]).

However, as is argued in the caption of Fig. 24, the TLS might indeed be the forthcomers of the  $O^-$  dangling bonds sitting at the RER-void fuzzy interface which as temperature decreases gets to shrink further and further (see Section B). In fact, the TLS concentration increases in glasses at the lowest temperatures [35]. Then, as temperature decreases the  $O^-$  ions get closer and closer together and the whole of the fluid contained in each void might become so strongly correlated that 3D coherent tunneling takes place. Therefore, the turning-up of the intrinsic magnetisation at the lowest temperatures for BAS-glass (and maybe

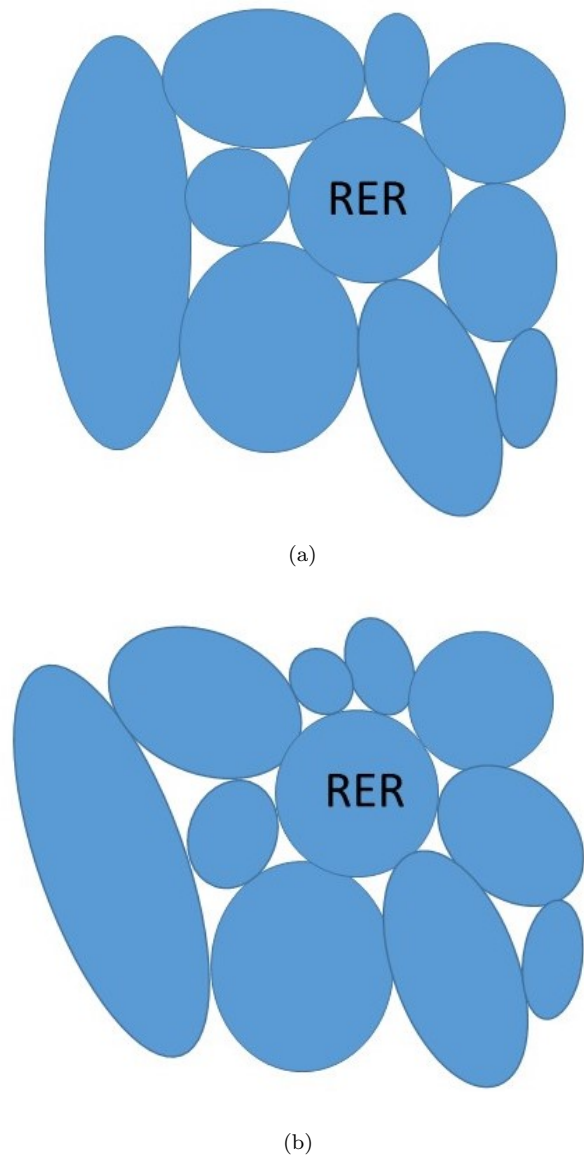


Figure 22: (a) 2D cartoon of a (portion of) medium-range RER-cell structure of our model glass, at some temperature  $T_1$  below  $T_g$ . The (blue) ovals are better-ordered RER (solid-like particle regions) and contain (white) in-between liquid-like regions. (b) The same as in (a), but for a different, close temperature  $T_2$ : the RER have moved to a new equilibrium configuration, changing the RER-RER voids’ total perimeter length per unit area (proportional to the intrinsic magnetisation) slightly.

also for BK7-glass) signals a 2D-3D dimensional local-to-global crossover. At even lower temperatures, the tantalising possibility that the whole network of  $O^-$  tunneling-ions-filled “voids” between the RER might become coherent would represent an extraordinary realisation of a natural quantum computer core containing some  $O(10^{17}) g^{-1}$  qubits (order of magnitude of  $n_{ATS}$ ). More investigations are under way.

### G. Final Conclusions, Authors and Acknowledgements.

As argued at length in this work, the phenomenon of *glass paramagnetism* is a reality and an unexpected new finding in the physics of glass with deep-reaching consequences for glass science in general. It is lamentable that it has been discovered in systems, the multi-silicates, where the level of Fe-impurity doping is always quite high so that Langevin paramagnetism has to be subtracted away. Better would be to conduct a systematic SQUID-magnetometry study in iron-group-free glass-forming systems like glycerol ( $C_3H_8O_3$ ), with a  $T_g$  of around 190 K. However: 1) inserting the substance at the liquid state in the sample-holder is problematic (the container vessel is also made of a type of glassy material); 2) the resulting magnetisation is likely to be very very weak, because of the large size of the RER in the organic glasses [28]; 3) there is very little knowledge about the values of the ETM parameters for glassy glycerol, none for other systems.

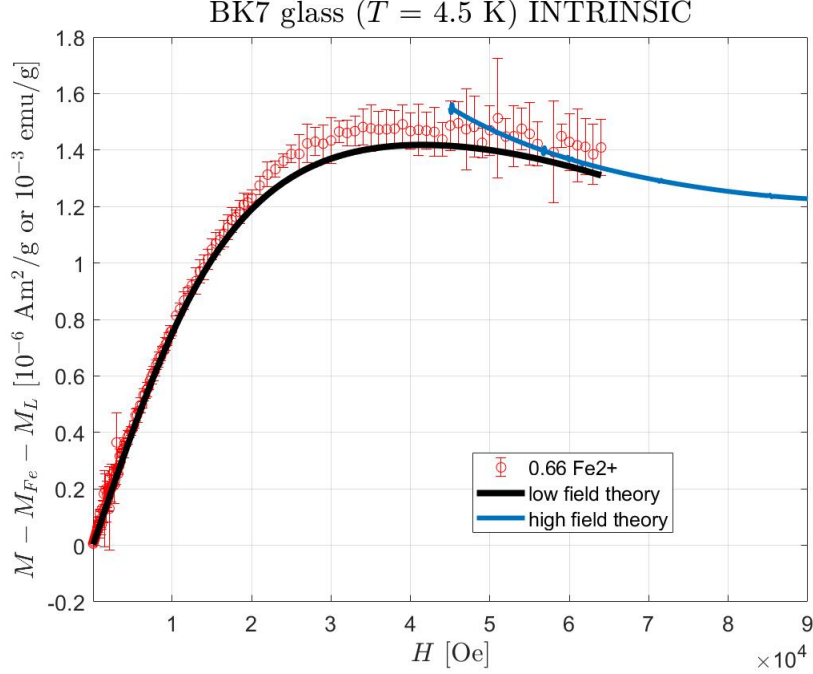


Figure 23: Data for the subtracted (of  $M_{LL}$  as in Eq. (1) PA) intrinsic magnetisation for BK7 glass at 4.5 K. The data are reasonably well explained by our ETM theory, using the low- and intermediate-field approximation and the high-field approximation. The combined approximations give a conclusive descent for high values of  $H$  after a Curie-like linear increase and broad peak due to the non-linear magnetic spectrum (Fig. 7(c), left panel, in the PA). The phenomenon of intrinsic glass paramagnetism is thus completely new.

We have thus chosen the multi-silicates because there has been extensive study of their unusual magnetic effects at low temperatures. Notice that ultra-pure silica glass (amorphous  $\text{SiO}_2$ ) is on the other hand likely to be characterised by very small-sized RER because it is a mono-component glass-forming substance with  $O(1)$  nm-size dynamical heterogeneities [17]. Therefore, the  $\text{O}^-$  dangling bonds on the RER surfaces will be strongly-correlated but too few in numbers ( $N_{tunn} \sim O(10)$ ), contrary to the case of the multi-silicate glasses. Consequently, as experimentally observed [41], there are no relevant magnetic-tunneling effects to be expected for *pure*  $\alpha\text{-SiO}_2$ : they would be far too weak to be measurable because  $N_{tunn}$  enters to the power 3 in the combination  $D_{0min,max} S_{\Delta} |Q/e| \propto N_{tunn}^3 \Delta_{0min} a_0^2$  (Section B, recall that for the multisilicates  $N_{tunn} \sim O(100)$  instead).

Authors: this part of the work has been written up entirely by the PI (GJ) who is the owner of the ETM-theory, of the calculations and carried out the data analysis and interpretation. As in the case of the PA, the qualitative MS chemical analysis was carried out by SR.

Acknowledgements: the PI is very grateful to Giacomo Marcon for help in working out the high-field behaviour of the intrinsic magnetisation. Also, the PI is grateful to Silvia Bonfanti for technical help and especially to Nika Frančeskin for encouragement in the completion of this work. Support by the INFN-Sezione di Pavia is also gratefully acknowledged.

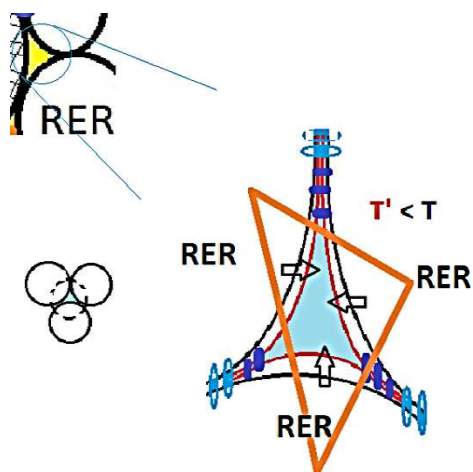


Figure 24: [What may really happen inside a RER-void (3D picture seen from above as in the schematic packing of spheres)]. The microscopic origin of the ATS and of the TLS in bulk glasses: growth of the RER-RER interface through consolidation at the expense of the RER-void’s mobile particles (from black- to red-lines). As temperature lowers from  $T$  to  $T' < T$ , the RER grow (arrows) into the “void” through adsorption of void’s particles, so that the surface available to  $O^-$  dangling bonds diminishes (light-blue area) while some more of the oxygens (dark-blue elements) end up as TLS in the RER-RER interface, which grows (zipping-up mechanism for the RER-RER interface). The orange triangle is schematic for the ATS quasiparticle (elementary excitation of the light-blue  $O^-$  region) three-welled potential.

## References

[\*] email: giancarlo.jug@uninsubria.it (corresponding author)

- [1] G. Jug and S. Recchia: Revealing the Intrinsic Magnetism of Non-Magnetic Glasses, arXiv:2111.00614 [cond-mat.mes-hall] (2021). Referred to here as the PA.
- [2] W.H. Zachariasen: The Atomic Arrangement in Glass, *J. Am. Chem. Soc.* **54**, 3841–3851 (1932); *ibid.*: The Vitreous State, *J. Chem. Phys.* **3**, 162–163 (1935).
- [3] B.E. Warren: The Diffraction of X-Rays in Glass, *Phys. Rev.* **45**, 657–661 (1934).
- [4] N. Valenkov and E. Porai-Koshits: Röntgenuntersuchungen des glasartigen Zustands (X-ray Investigations of the Glassy State), *Z. Kristallogr.* **95**, 195 (1936).
- [5] A.A. Lebedev: Struktura stekol po dannym rentgenostrukturnogo analiza i issledovaniya opticheskikh svoystv (The structure of Glass according to X-ray Analysis and Studies of the Optical Properties), *Izv. Akad. Nauk SSSR Ser. Fiz. (Bull. Acad. Sci. USSR, Phys. Ser.)* **4**, 584 (1940).
- [6] E.A. Porai-Koshits: Genesis of Concepts on Structure of Inorganic Glasses, *J. Non-cryst. Sol.* **123**, 1–13 (1990).
- [7] P.H. Gaskell: The Structure of Simple Glasses: Randomness or Pattern-the Debate Goes on, *Fiz. Khim. Stekla* **24**, 266-277 (1998); [Engl. Transl.: *Glas. Phys. Chem.* **24**, 180-188 (1998)].
- [8] A.C. Wright: Crystalline-like Ordering in Melt-quenched Network Glasses? *J. Non-Cryst. Solids*, **401** 4–26 (2014); *ibid.*: The Great Crystallite versus Random Network Controversy: A Personal Perspective, *Int. J. Appl. Glass Sci.* **5**, 31–56 (2014).

- [9] G.N. Greaves: EXAFS and the Structure of Glass, *J. Non-Cryst. Solids* **71**, 203-217 (1985).
- [10] A.S. Bakai: The Polycluster Concept of Amorphous Solids, Beck/Günterodt (Eds.), *Metallic Glasses I*, Topics in Applied Physics **72** (Springer-Verlag, Berlin Heidelberg 1994), p. 209–255.
- [11] A.S. Bakai: *Poliklastern'ie Amorfn'ie Tela* (Khar'kov "Synteks", Khar'kov, Ukraine, 2013) (in Russian).
- [12] G. Jug: The Polycluster Theory for the Structure of Glasses: Evidence from Low Temperature Physics, in: *Modern Problems in Molecular Physics: Selected Reviews*, L. A. Bulavin and A. V. Chalyi (eds.), Springer International Publishing AG (2018), Ch. 13.
- [13] W. Vogel, L. Horn, H. Reiss and G. Volksch: Electron-Microscopical Studies of Glass, *J. Non-Cryst. Solids* **49**, 221-240 (1982).
- [14] W. Vogel: *Glass Chemistry* (2nd edn., Springer, Berlin 1992), p. 74.
- [15] W. Vogel: *Structure and Crystallisation of Glasses* (Edition Leipzig, Pergamon Press, Oxford 1971).
- [16] J. Zarzycki: *Glasses and the Vitreous State* (Cambridge University Press, Cambridge 1991).
- [17] G. Jug, A. Loidl and H. Tanaka: On the Heterogeneities of Glass-Forming Liquids and Glasses, *EPL* **133**, 56002 (2021).
- [18] G. Jug and M. Paliienko: Multilevel Tunneling Systems and Fractal Clusters in the Low-Temperature Mixed Alkali-Silicate Glasses, *Sci. World J.* **2013**, 1–20 (2013).
- [19] G. Jug, S. Bonfanti and W. Kob: Realistic Tunneling Systems for the Magnetic Effects in non-metallic Real Glasses, *Phil. Mag.* **96**, 648–703 (2016).
- [20] A theoretical derivation of Eq. (3) beginning from the more microscopic Hamiltonian Eq. (2) is possible and will be published in due course (see however also the Appendix in [18]).
- [21] P. Esquinazi (Ed.): *Tunneling Systems in Amorphous and Crystalline Solids* (Springer, Berlin, 1998).
- [22] T. Kawasaki, T. Araki and H. Tanaka: Correlation between Dynamic Heterogeneity and Medium-Range Order in Two-Dimensional Glass-Forming Liquids, *Phys. Rev. Lett.* **99**, 215701 (2007).
- [23] T. Kawasaki and H. Tanaka: Structural origin of dynamic heterogeneity in three-dimensional colloidal glass formers and its link to crystal nucleation *J. Phys.: Condens. Matter* **22**, 232102 (2010).
- [24] G. Jug: Theory of the Thermal Magnetocapacitance of Multi-component Silicate Glasses at Low Temperature, *Phil. Mag.* **84**(33), 3599–3615 (2004).
- [25] S. Bonfanti: Low temperature theoretical and numerical study of structural glasses (Ph.D. Thesis, Università degli Studi dell'Insubria, 2015) <http://insubriaspaces.cineca.it/handle/10277/597>
- [26] J. A. Sussmann: Electric Dipoles due to Trapped Electrons, *Proc. Phys. Soc. (London)* **79**, 758–774 (1962).
- [27] S. Bonfanti and G. Jug: On the Paramagnetic Impurity Concentration of Silicate Glasses from Low-Temperature Physics, *J. Low Temp. Phys.* **180**, 214–237 (2015).
- [28] M. Paliienko: Multiple-welled Tunneling Systems in Glasses at low Temperatures (Ph.D. Thesis, Università degli Studi dell'Insubria, 2011) <http://insubriaspaces.cineca.it/handle/10277/420>
- [29] N.W. Ashcroft and N.D. Mermin: *Solid-State Physics* (Saunders College International, Philadelphia 1976).
- [30] G. Jug: Multiple-well Tunneling Model for the Magnetic-field Effect in Ultracold Glasses, *Phys. Rev. B* **79**, 180201 (2009).
- [31] G. Jug, M. Paliienko and S. Bonfanti: The Glassy State — Magnetically Viewed from the Frozen End, *J. Non-Cryst. Solids* **401**, 66–72 (2014).

- [32] T. Herrmannsdörfer and R. König: Magnetic impurities in glass and silver powder at milli- and microkelvin temperatures, *J. Low Temp. Phys.* **118**(1–2), 45–57 (2000).
- [33] G. Jug, G. Prando and P. Carretta (in preparation, 2021).
- [34] G. Jug, P. Sala, S. Recchia, G. Vesco and L. Nardo (in preparation, 2021).
- [35] R.B. Stephens and Xiao Liu: *Low-Energy Excitations in Disordered Solids* (World Scientific, Singapore 2021).
- [36] G. Jug: The Making of a Theory of the Vitreous Solid State: “From 1 mK to 1 kK”, in: *2019 Sustainable Industrial Processing Summit and Exhibition, Vol. 1: Angell Intl. Symp. - Molten Salt, Ionic & Glass-forming Liquids*, Edited by F. Kongoli et. al. (FLOGEN Stars Outreach 2019).
- [37] B. Ruta, G. Baldi, Y. Chushkin, B. Rufflé, L. Cristofolini, A. Fontana, M. Zanatta and F. Nazzani: Revealing the Fast Atomic Motion of Network Glasses, *Nature Comms.* **5**, 3939 (2014).
- [38] G. Marcon: The Intrinsic Magnetisation of Non-magnetic Glasses: An Improved Theory (M.Sci. Thesis, Università dell’Insubria 2021).
- [39] G. Jug and M. Paliienko: Evidence for a Two-component Tunnelling Mechanism in the Multicomponent Glasses at low Temperatures, *Europhys. Lett.* **90** 36002 (2010).
- [40] K.H. Fischer and J.A. Hertz: *Spin Glasses* (Cambridge UP, Cambridge 1991).
- [41] S. Ludwig, P. Nagel, S. Hunklinger, and C. Enss: Magnetic Field Dependent Coherent Polarisation Echoes in Glasses, *J. Low Temp. Phys.* **131** 89–111 (2003).